# IDENTIFYING SUB-NETWORKS IN NEURAL NETWORKS VIA FUNCTIONALLY SIMILAR REPRESENTATIONS

**Anonymous authors**
Paper under double-blind review

## ABSTRACT

Mechanistic interpretability aims to provide human-understandable insights into the inner workings of neural network models by examining their internals. Existing approaches typically require significant manual effort and prior knowledge, with strategies tailored to specific tasks. In this work, we take a step toward automating the understanding of the network by investigating the existence of distinct sub-networks. Specifically, we explore a novel automated and task-agnostic approach based on the notion of functionally similar representations within neural networks, reducing the need for human intervention. Our method identifies similar and dissimilar layers in the network, revealing potential sub-components. We achieve this by proposing, for the first time to our knowledge, the use of Gromov-Wasserstein distance, which overcomes challenges posed by varying distributions and dimensionalities across intermediate representations—issues that complicate direct layer-to-layer comparisons. Through experiments on algebraic, language, and vision tasks, we observe the emergence of sub-groups within neural network layers corresponding to functional abstractions. Additionally, we find that different training strategies influence the positioning of these sub-groups. Our approach offers meaningful insights into the behavior of neural networks with minimal human and computational cost.[1]

## 1 INTRODUCTION

Rapid progress in transformer language models has directed attention towards understanding the underlying causes of new capabilities. Like many other neural methods, large language models (LLMs) are mostly black-box models and explainable artificial intelligence aims to offer insights and improve human understanding of these LLMs. Recently, mechanistic interpretability research has gained popularity, focusing on reverse-engineering models into human-understandable algorithms, using methods such as computational graphs and circuits (Nanda et al., 2023; Conmy et al., 2024). Examples include recovering internal mechanisms of LLMs to solve typical mathematical problems such as modular sum (Zhong et al., 2024).

Current approaches primarily rely on extensive manual inspection and trial-and-error to reverse engineer networks by discovering a sequence of learned functions that produce a desired output. This process requires significant human prior knowledge with strategies tailored to specific tasks such as algebraic problems (Charton, 2023). Automatic discovery of these functions is a difficult task due to the large search space involved. We investigate a simpler task that can be considered as an initial step towards automating the discovery of these functions: *is it possible to detect how many distinct (complex) functions exist in a learned network, and which layers correspond to each such function?* Understanding neural networks through the identification of subnetworks is essential due to the complexity and opacity of modern deep learning models. Neural networks, especially those with many layers and parameters, often exhibit behaviors that are difficult to interpret holistically. Identifying subnetworks allows us to break down the model into smaller, more interpretable units, providing insights into how individual components contribute to the model's overall performance. In this paper, we take such a step towards an automatic and task-agnostic approach to identify sub-components in neural networks that are functionally different from each other. Specifically, we treat the intermediate layers of neural networks as computing different *functions* of the input and base

[1] Code will be made publicly available.

our approach on *functional similarity*. These distinctive subnetworks would represent one function in a sequence of different ones, and knowing such a partition would facilitate further decoding these functions leading a better understanding of the network.

The nature of functional similarities differ depending on which of the two cases is true: either we have a hypothesized target function that part of the network may (approximately) compute, or we lack such a hypothesis. In the case of a given target function, functional similarity relates to the output of the target function, and the problem is one of search to find a network layer that best approximates it. This is akin to comparing two functions based on the values they take for the same input samples. The use of probes attached to representations is a popular method for detecting such similarities.

The more realistic case with neural networks is the absence of a target function, which is the primary focus of this paper. In this case, we propose to measure the functional similarity *between* layers of the network, and the problem is to identify distinctive sub-components within the network by finding which layers are functionally less similar to previous layers as shown in Figure 1. The idea is that less similar layers (brighter colors) may indicate boundaries of a sub-component, while more similar layers (darker colors) likely belong to the same sub-component. While it may be tempting to also use probes here for layer comparisons, the lack of targets makes it unclear how the representations in these layers should be transformed by the probes for comparison. We need a more direct way to compare these representations. Hence, we propose to measure similarity using Gromov-Wasserstein (GW) distance (Zheng et al., 2022) between representations from different layers of the network. As elaborated further in Section 4.1, GW allows distance computation between distributions supported on two different metric spaces with different supports and potentially different dimensions, which is common across different layers in neural networks. GW is also invariant to permutation of the representation within a layer, a crucial property since neural networks are known to have permutation symmetries (Goodfellow et al., 2016). As such, GW can effectively identify genuinely distinct behaviors across (groups of) layers.

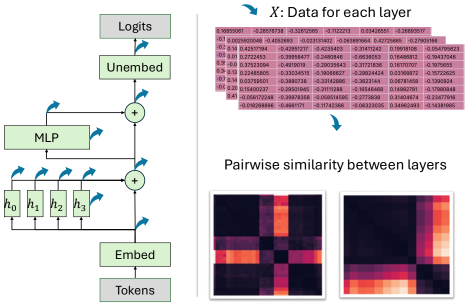

Figure 1: Overview of our approach where we use representations to identify functionally distinct sub-networks (darker blocks) leveraging GW distance.

We validate our approach on algebraic, NLP, and vision tasks, showing that GW distance provides a systematic way to analyze and identify subnetworks. Additionally, our findings provides a holistic view on differences in representations of models trained with different strategies. We observe clear patterns in the form of block structures among different layers, suggesting there exist sub-networks that have different functions, particularly at the transition layers where major functional changes may occur. Moreover, the GW distance can also be used to observe the emergence of subnetworks during training process. Overall, we hope that our method can improve the efficiency of mechanistic interpretation by finding subnetworks in larger models, reducing the need for extensive human effort and potentially contributing to a further understanding of neural network behaviors.

## 2 Background and Related Work

With its popularity, mechanistic interpretability has become a disparate area, with many different applications in vision (Palit et al., 2023), and language (Ortu et al., 2024; Hernandez et al., 2023; Yu et al., 2024), and we survey various directions within it.

**Algorithm discovery in algebraic problems** Modular sum algorithms (Nanda et al., 2023) are studied in the context of progress measure in emerging abilities of transformers. The authors in (Zhong et al., 2024) show, via various inspection such as gradient symmetry, logit patterns, and input pair relations, that one class of algorithm is preferred than another. Other math problems such as the greatest common divisor (Charton, 2023) also show insights into the inner mechanisms of neural networks. However, most of these works require extensive human effort to reverse engineering these algorithms. We investigate whether we can automate the discovery process by studying a simpler problem of sub-function detection.

**Subnetwork Discovery** Automated circuit discovery (Conmy et al., 2024; Shi et al., 2024) intends to find a computational graph that is far sparser without sacrificing performance. Heuristic Core (Bhaskar et al., 2024) hypothesizes that there exists a set of attention heads that encompasses all subnetworks, learning shallow and non-generalizable features. Moreover, various work have explored neuron semantics and possible disentanglement of semantics (Bricken et al., 2023; Dreyer et al., 2024; Huang et al., 2024a), as well as concept representations (Park et al., 2024). Instead of studying circuits and neuron, we investigate differences among neural network layers as a whole, based on an existing line of work (Nanda et al., 2023). Block structures within neural network have been observed in previous studies (Nguyen et al., 2022).

**Methods of Studying Mechanisms** Weight inspection and manipulation are commonly employed techniques to gain insights into the inner work of networks, including studying periodicity (Nanda et al., 2023) and weight gradients (Zhong et al., 2024). Modifying or ablating the activation of a specific model components (Huang et al., 2024b; Kramár et al., 2024), including attention knockout (Wang et al., 2022), and even direct modification of attention matrix (Ortu et al., 2024; Geva et al., 2023) are prevalent. Another popular approach involves representation and output inspection (Meng et al., 2022), including logit patterns (Zhong et al., 2024), residual stream (Ortu et al., 2024), and periodicity (Nanda et al., 2023). Causal mediation analysis is used to compute the indirect treatment effect (Meng et al., 2022; Yu et al., 2024) with perturbed embedding. Rather than just inspection of outputs, many works have proposed to map the output to some target and is a popular technique for analyzing how neural activations correlate with high-level concepts (Huang et al., 2024a). Linear probes are generally used. (Hou et al., 2023) uses a nonparametric probe ($k-$nearest-neighbor) to classify outputs for reasoning tasks. We focus on using similarity measure between layers here.

**Similarity Measure between Neural Network Layers** There are studies that quantify the similarity between different groups of neurons (Klabunde et al., 2023), typically layers (Ding et al., 2021), to understand and compare different neural networks. Cross product between each layer output and final output (Yu et al., 2024) is used to approximate each layer's contribution to the final prediction. Generally a normalized representation is used to compare different transformer blocks, with different desired invariance properties, such as invariance to invertible linear transformation in canonical correlation analysis (Morcos et al., 2018), orthogonal transformation, isotropic scaling, and different initializations in centered kernel alignment (Kornblith et al., 2019). Other measures include representational similarity analysis (Mehrer et al., 2020), which studies all pairwise distances across different inputs. Wasserstein distance has been explored in measuring similarities in the context of neural networks (Dwivedi & Roig, 2019; Cao et al., 2022; Lohit & Jones, 2022), but they assume that different layer representations belong to the same metric space, which is very unlikely even if they have the same dimensionality as the semantics captured by each layer are likely to differ significantly. Several similarity measures (Tsitsulin et al., 2019; Demetci et al., 2023a) are related to GW distance. While GW distance has been used for model merging as a regularization (Singh & Jaggi, 2020; Stoica et al., 2023), it has not been fully explored in the area of mechanistic interpretability, particularly for the subnetworks identification.

## 3 Functional Similarity Within Neural Networks

We aim to identify sub-components of a neural network based on their mechanistic functions. When we have a hypothesized target function that the sub-component may compute, this can be formulated as a similarity search problem. In this context, we search for candidate representations within neural networks' outputs that represents changes in function computation. The search problem consists of three key elements: the search space, the search target, and the similarity measures used to evaluate how closely the candidates in the search space match the target.

### 3.1 Similarity Measures

Let $f : X \rightarrow Y$ be a function that map $x$ in a set of input $X = \{x_i : x_i \in \mathbb{R}^{d_x}\}_{i=1}^n$ to $y$ in a set of output $Y = \{y_i : y_i \in \mathbb{R}^{d_y}\}_{i=1}^n$. Each element in $Y$ and $X$ are assumed to be a vector with dimensions $d_y$ and $d_x$, respectively, with $n$ being the set size, without loss of generality. Let $f_0 : X \rightarrow Y^0$ be another function that produces $Y^0 = \{y_i^0 : y_i^0 \in \mathbb{R}^{d_y}\}_{i=1}^n$ given $X$. Note sets can be concatenated into matrix forms as $Y^0, Y \in \mathbb{R}^{n \times d_y}$ and $X \in \mathbb{R}^{n \times d_x}$.

**Functional Similarity.** Similarity between two functions, $f_0$ and $f$, over a set of input $X$, can be measured by the similarity between their output sets $Y_0 = f_0(X)$ and $Y = f(X)$.

We can use a scoring or distance function $D(Y^0, Y)$ as a measure between output similarity and hence the functional similarity between $f_0$ and $f$, where we regard $Y^0$ as the function/search target. If they are close according to $D$, then the function values should be similar to each other locally at a set of points $X$. Otherwise, these functions should be different at $X$. Popular measures such as Euclidean distance have been used for this purpose (Klabunde et al., 2023). Each intermediate representations of a neural network can be naturally treated as function outputs, given inputs $X$.

**The Need for Complex Functional Similarity Measure.** Since we cannot exactly control the behavior of a trained neural network, the layer-wise functions $f$ that it learns can be complex and thus the learned representation $Y$ from each layer may be a complex function of the target $Y^0$ rather than a simpler transformation. For example, let $Y^0 = \sin(X)$ and a candidate $Y = \sin^2(X) = (Y^0)^2$. They share strong similarity, but a linear transformation will not be able to capture their functional similarity. If we want to truly understand where function $f_0$ might be approximately computed, we should consider functions of target $Y^0$, but naively listing out all possibilities can be prohibitive. As a consequence, one may need to use more complex measures to deal with such a space.

### 3.2 Search Space

We consider multiple candidate $Y$'s to form the search space for target $Y^0$. In the context of MLP neural networks for example, where $\sigma(.)$ denotes the non-linearity and $W$s are the parameter matrices, we have $Y^* = W_n(\sigma(W_{n-1} \ldots \sigma(W_1 X)))$ for the whole network. We can extract many $Y$'s from intermediate functions of the model, for instance $Y_1 = W_1 X$, $Y_2 = \sigma(W_1 X)$, and so on. These $Y$'s are often called representations, activations, or sometimes even "outputs" from each layer. We use these terms interchangeably here. For attention modules in transformer neural networks (Vaswani et al., 2017), we can similarly extract $Y$'s from attention key, query, and value functions as well as MLP functions. We list the exact equations and locations of representations considered in the transformer models in Table 2 in Appendix A, which serves as the focus of this paper. To show the method is applicable to other types of networks, we also consider convolutional neural networks with residual layers, with candidate representations listed in Table 3 in in Appendix A.

### 3.3 Search Targets

**Known Targets** When the search target, denoted as $T$, is a value from a known function, we can directly compare outputs between representations from each layer and known function output $T$. Representations from each layer can be directly compared with the target via a probe. Popular linear probes can be used to assess the similarity between a target and any layer's representation. For instance, linear regression can be used to model each target $T$ from each representation candidate $Y$, and the residual error is used as the search criteria between $Y$ and $T$. As discussed previously, to deal with the potentially large search space of functions of the target, a more powerful probe (such as a nonlinear MLP function) may have to be used so that it can detect more complex similarities to $T$.

One challenge with using predictive probes to compute the distance measure $D$ is that the target function must be known. In practice, however, we often lack knowledge of specific targets. While it's possible to experiment with various target functions with power probes, the vast number of potential targets makes this approach inefficient. This calls for an alternative strategy to distinguish sub-components in a network through representation similarity.

## 4 Gromov-Wasserstein Distance as a Similarity Measure

**Unknown Targets** When the search target is unknown, functionally similar parts cannot be identified by comparison to a predefined set of target functions. Instead, we propose to identify the similarities and subnetworks among the representations at each intermediate layer. Each layer, however, posits a representation that potentially has a different distribution, not to mention even different dimensionality depending on the architectures and layers one considers (viz. mlp_in layer and attention layer in transformer blocks). Consequently, representations across layers may be incomparable using standard distance metrics, such as the $\ell_p$ norm amongst others.

To overcome these challenging issues, we propose computing distances between representations produced at the same layer for different inputs and match the vertices of this weighted graph – where each dimension of the representation of the inputs are vertices and the distances indicate weights on the edges – with the vertices of a similarly constructed weighted graph from another layer. Essentially, we assume the representations in a layer are samples of the underlying distribution, and we want the best permutation of representation dimensions in one layer that aligns with vertices in another layer, thereby deriving the inter-layer distance. If this inter-layer distance is low, then the two layers we consider to be functionally similar, given the same input data.

Formally, without loss of generality, let $Y_1 = \{y_{1i} : y_{1i} \in \mathbb{R}^{d_1}\}_{i=1}^{n}$ and $Y_2 = \{y_{2i} : y_{2i} \in \mathbb{R}^{d_2}\}_{i=1}^{n}$ be representations of $n$ examples from two different layers, where the discrete distributions over the representations are $\mu_1$ and $\mu_2$ respectively, with dimension $d_1$ possibly being different from $d_2$. Direct distance computation between them is not reasonable. Instead, we seek to compute a coupling or matching $\pi \in \Pi(\mu_1, \mu_2)$ between the $n$ examples in each set such that given the pairwise distances $D_1, D_2 \in \mathbb{R}^{n \times n}$ within representations $\boldsymbol{Y}_1$ and $\boldsymbol{Y}_2$ respectively, the sum of differences between the distances of the matched examples is minimized. Loosely speaking, we aim to find a matching that preserves the pairwise distance as much as possible. In particular, we want to minimize the following:

$$\rho(\boldsymbol{Y}_1, \boldsymbol{Y}_2, \mu_1, \mu_2, D_1, D_2) \triangleq \min_{\pi \in \Pi(\mu_1, \mu_2)} \sum_{i,j,k,l} (D_1(i,k) - D_2(j,l))^2 \pi_{i,j} \pi_{k,l}$$

$$\text{s. t.} \quad \pi \boldsymbol{I} = \mu_1; \pi^T \boldsymbol{I} = \mu_2; \pi \geq 0. \tag{1}$$

It turns out that $\rho$ corresponds to the Gromov-Wasserstein (GW) distance (Demetci et al., 2023b), used to map two sets of points in optimal transport. We thus utilize this distance as a measure of inter-layer functional similarity in the setting where the target is unknown.

### 4.1 Justification for GW Distance as a Functional Similarity Measure

Let $(\boldsymbol{Y}_1, D_1, \mu_1)$ and $(\boldsymbol{Y}_2, D_2, \mu_2)$ be two given metric measure space (mm-space), where $(\boldsymbol{Y}, D)$ is a compact metric space and $\mu$ is a Borel probability measure with full support: supp$(\mu) = \boldsymbol{Y}$. An isomorphism between $\boldsymbol{Y}_1, \boldsymbol{Y}_2$ is any isometry $\Psi : \boldsymbol{Y}_1 \rightarrow \boldsymbol{Y}_2$, i.e., a distance-preserving transformation between metric spaces, such that $\Psi_{\#\mu_1} = \mu(\Psi^{-1}) = \mu_2$.

**Theorem 4.1.** *(Mémoli, 2011). The Gromov-Wasserstein distance in equation 1 defines a proper distance on the collection of isomorphism classes of the mm-spaces.*

*Remark.* The Gromov-Wasserstein distance itself is defined on isomorphism-classes of metric measure spaces, which means that any distance preserving (isometric) transformation of a space should preserve GW distance between the points in that space and any other space (Mémoli, 2011). These isometric transformations include rigid motions (translations and rotations) and reflections or compositions of them. Additionally, permutations of points in a space also preserve GW distances, as the points are unlabeled. Hence, GW distance captures much richer transformations across layers.

The computed GW distance represents the minimal distance over all possible transportation plans between two sets of points from different spaces. In our context, we can also view GW as a measure that quantifies the distance between distance-based (i.e., Euclidean-distance) graphs, with a set of points as its nodes. Hence this would be low if the graph undergoes (nearly) isomorphic transformations between layers. Conversely, a high GW distance indicates a non-distance preserving transformation across layers, potentially reflecting a highly non-linear operation. While GW distance does not reveal the exact function operation, it highlights specific layers for further investigations.

**Favorable Properties of GW.** Besides the above noteworthy property of GW to map between different spaces, it also has other favorable properties (Zheng et al., 2022; Demetci et al., 2023b): i) It is symmetric and satisfies triangle inequality. ii) It is invariant under any isometric transformation of the input, which is advantageous because we do not want rotations and reflections to affect our similarity search. This invariance also includes permutation invariance, which is a beneficial property since we want the distance between layer representations to remain unaffected by permutations within the representations in each layer. iii) GW is scalable since it does not require estimating high-dimensional distributions, which is often the case with intermediate representations in large models; instead, it only compare them to obtain a distance measure. iv) GW is monotonic in (positive) scaling of pairwise distances, and hence the same layers should appear to be closer than others even with scaling.

**Distance Distributions.** As an illustrative example, we plot the histogram on pairwise distances for a batch of samples across all transformer blocks in BERT models from the YELP review dataset in Figure 2. For more details on YELP, we provide a comprehensive discussion in the experiments section 5.2. The results in Figure 2 show the distributions on pairwise distances begin to differ from block 9, consistent with GW distance observed in Figure 6 suggests that significant transformations occur and can be effectively captured by GW. We include the full results and discussion in Appendix F.

**Neighborhood Change.** Complementary to the distribution of pairwise distances, the changing representations of samples could also alter their relative neighborhoods across transformer blocks. We plot a tSNE projection (Van der Maaten & Hinton, 2008) of representations from a batch of samples on YELP, and visualize it in Figure 11e of Appendix F. The Jaccard similarity, measuring the overlap between top-5-neighbors of 3 selected samples across different transformer blocks, ranges from 0.0 to 0.43, with average values of $\{0.27, 0.26, 0.26\}$. The full details are shown in Table 5 of Appendix F. Hence, the sample neighborhood changes across blocks, which can be indicative of functional changes that are not captured by comparing distributions alone. However, GW can account for such changes as well.

**Computation Details.** We use an existing optimal transport toolbox, `pythonot` (Flamary et al., 2021), for computing GW distance. Specifically, we use an approximate conditional gradient algorithm proposed in (Titouan et al., 2019), which has a complexity of $O(mn^2 + m^2n)$, where $m$ and $n$ are the dimensions of two spaces (here the number of data samples from two layers being compared). In comparison, the Wasserstein distance Lohit & Jones (2022) may require $O(n^3 log(n))$ for exact computation. When the dataset is large, we can also subsample the dataset to improve the computational efficiency.

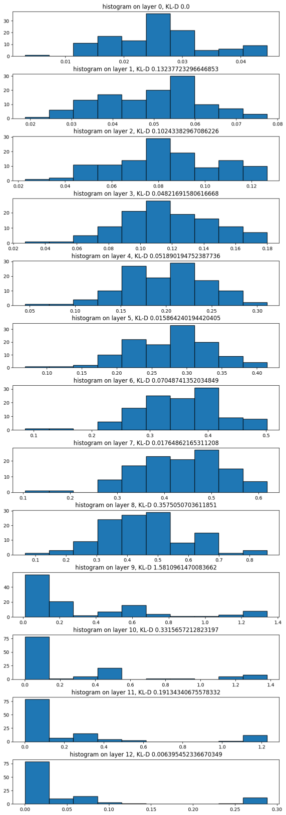

Figure 2: Histogram on pairwise distances for outputs from all transformer blocks in a fine-tuned BERT model trained on YELP dataset.

## 5 Empirical Study and Findings

We compare the proposed similarity measure for sub-network identification against a set of baselines across multiple datasets, including those from algebraic operation, NLP, and computer vision tasks. For a list of baselines with their implementation details, please see Appendix H.

### 5.1 Synthetic Modular Sum Tasks

We begin by validating the Gromov-Wasserstein distance by comparing it against known partitions of the networks to determine whether it can successfully identify sub-networks. We first introduce the setup for the experiment, including data generation and models to be investigated.

**Setup** As a test case, we focus on a modular sum problem, following existing works (Nanda et al., 2023). We consider two datasets: the first generated by a single modular sum function with $c = f_{\text{mod}}(a + b) = (a + b)\text{mod p}$, where $a, b, c = 0, 1, \ldots, p - 1$, with $p = 59$. The second dataset is more complex, with $c = f_{\text{mod3}}(a, b)$ of three levels of modular sums, namely: $c_1 = (a + b)\text{mod } p_1, c_2 = (c_1 + b)\text{mod } p_2, c = (c_2 + b)\text{mod } p_3$, where $p = [59, 31, 17]$.

**Training procedure** We train 3 different neural networks with transformer blocks to predict $c$ given $(a, b)$. These networks contain input embeddings for $a$ and $b$, each of size $d$, i.e., $[\boldsymbol{E}_a, \boldsymbol{E}_b] \in \mathbb{R}^{2d}$, and predict a categorical output $c$ via an unembedding/decoding layer. All parameters in the network are learned. For the first simpler $f_{\text{mod}}$ dataset, we train a neural network consisting of a one-block ReLU transformer (Vaswani et al., 2017), following the same protocol and hyperparameter choices as previous works (Nanda et al., 2023; Zhong et al., 2024). We call this **Model 0**. For the more complex $f_{\text{mod3}}$ dataset, we train two neural networks consisting of three-block ReLU transformers, with 3 transformer blocks corresponding to the three levels of modular sum functions, and 4 attention

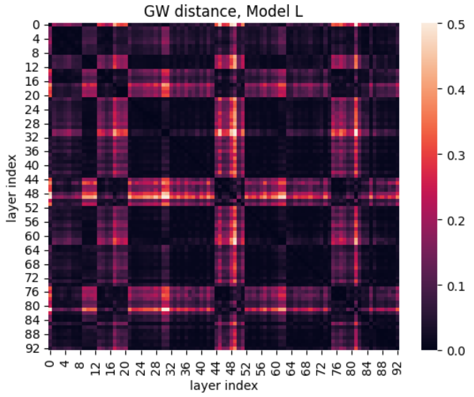

Figure 3: Model L (layer-wise training) pairwise GW distance, on $f_{\text{mod3}}$ dataset.

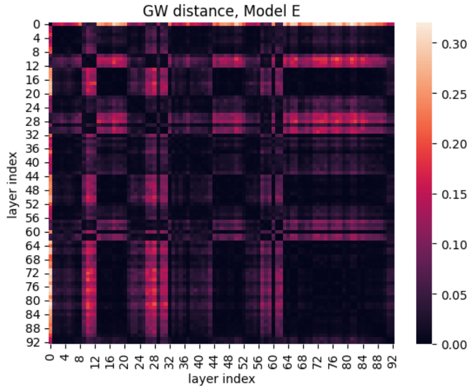

Figure 4: Model E (end-to-end training) pairwise GW distance, on $f_{\text{mod3}}$ dataset.

heads within each block. The first network, which we call **Model E**, employs an end-to-end training procedure to directly learn output $c$ given input $(a, b)$. For the second network, which we call **Model L**, we use the same architecture as Model E but with a layer-wise training approach instead of end-to-end training. Specifically, we use the following procedure:

1. We train the first transformer block of Model L to predict $(c_1, b)$ using an additional linear layer on top, given inputs $(a, b)$.

2. Once block 1 is fully trained, we discard the linear layer, freeze everything before the linear layer, and use its representations of $(c_1, b)$ to train the second block to predict $(c_2, b)$, again incorporating an additional layer on top.

3. Finally, we repeat the above step by freezing the first and second block and training the last block to predict $c$, using representations of $(c_2, b)$.

In all these models, we are able to achieve $100\%$ prediction accuracy on a separate validation dataset. Note that extra linear layers can also be considered as probes but used in training. More details can be found in appendix B. We use the GW measure on **Model L** with layer-wise training to verify if there is consistency between GW distances and known output $c$'s. To evaluate the capability of handling different dimensions, we directly measure GW distance between the 93 intermediate representation $Y$ (see appendix B for search space details) and $c$'s. To speed up computation of GW distance, we randomly sub-sample 1000 data from a total of 3600 samples, reducing time from 2 min to 5 seconds for each computation.

Table 1: Gromov-Wasserstein Distance Results for Various Targets, for $f_{\text{mod3}}$ dataset.

| Model L | GW-D for | Top Similar Layers | $D_{\text{min}} =$ |
|---|---|---|---|
| | $c_1$ | Resid-Post$^1$ | 0.02 |
| | $c_2$ | Resid-Post$^2$ | 0.03 |
| | $c$ | Resid-Post$^2$, Resid-Pre$^2$, Resid-Post$^3$, and 6 others | 0.04 |

**Results** The results are shown in the Table 1. We see that in the **Model L**, the GW distance correctly identifies the most similar layers in accordance with different intermediate $c$'s. The final target $c$ contains 9 similar layers all with distance around 0.04. In Appendix C, we also test probes since the targets are known. Results shows GW distance can be a reliable alternative to the probes.

Moreover, as previously mentioned GW distance can naturally compare representations across and within transformer blocks with different dimensions. In Fig 3 and Fig 4, we visualize the pairwise GW distance between layer representations without a target for **Model L** and **Model E**. Looking at **Model L** we see predominantly 3 groupings of layers: i) layers roughly from 20 to 44 are similar to each other and to layers 52 to 72, ii) layers roughly 12 to 19 are similar to each other and layers 45 to 51 and iii) the initial and last few layers are mainly similar to themselves. Interestingly, the number of groupings corresponds to the 3 functions trained layer-wise in **Model L**. We also observe differences in patterns across **Model L** and **Model E**, suggesting layer-wise and end-to-end training return different networks. Compared to the fixed layer-wise training, end-to-end training in **Model E** may learn faster in the earlier layers and may not have much to learn in later layers, as the function may not be particularly challenging for it. This could explain why, starting from layer 64, all layers in **Model E** exhibit similar representations. Moreover, magnitudes of the distances are also different, with **Model L** showing larger distances, indicating that learning the targets $c_1, c_2$ result in more functional differences. One possible explanation could be that **Model E** directly operates in the trigonometry space (Nanda et al., 2023), without having to predict the exact integer values until later, thereby suppressing the distances. We include results from baseline methods capable of handling different dimensions between subspaces in Appendix D.

To gain a deeper understanding of the operations within each transformer block, we visualize pairwise GW distances among layers for **Model 0** for dataset $f_{\text{mod}}$ in Figure 5. In this case, we have a total of 31 representations since only one transformer block is used. We notice the first major difference occurs between layers 13 and 16, which are 4 Attn-Pre (computing key and value product). The second difference occurs between layers 17 and 20, which are the first 3 Attn (computing $\boldsymbol{A}(\boldsymbol{X})$). This suggests that major computation seems to be done by the attention mechanism. Note that distances are not monotonically increasing across layers, which is expected as the representation spaces can change significantly given the heterogeneity of the operations such as those performed by residual connections and attention within a transformer block.

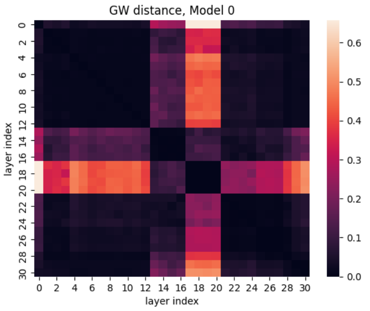

Figure 5: Model 0 Pairwise GW distance, on $f_{\text{mod}}$ dataset.

### 5.2 NLP Tasks

**Setup** We now apply GW distance to real natural language processing tasks. We experiment on benchmark sentiment analysis datasets, Yelp reviews and Stanford Sentiment Treebank-v2 (SST2) from the GLUE NLP benchmark (Wang et al., 2019), with the goal to predict of the text has positive or negative sentiment, and analyze how different layers from fine-tuning BERT(-base) (Devlin et al., 2019) models perform on these datasets. We use the pretrained BERT to generate 4 fine-tuned models, corresponding to a dense model and 3 sparse models with sparsity levels of 25%, 70% and 95% using a state-of-the-art structured pruning algorithm (Dhurandhar et al., 2024). Sparsity are used to force models to condense information into the limited remaining weights, enabling us to examine potential links between this constraint and their structural similarity. Training details are in Appendix E. Due to the size of BERT models, we limit our analysis to comparing the final representations from each of the 12 transformer blocks, rather than examining all intermediate representations within the blocks.

**Results** In the last row of Figure 6a, we see that the pre-trained BERT does not have major differences among blocks, which is not surprising given its accuracy on YELP is only 49.3% (roughly equivalent to random guessing). In Figures 6b to 6e, we see an interesting pattern emerge, revealing two-to-three major block structures in the (sparse) fine-tuned BERT models identified by our approach. The first major differences occur at block 9 and then the last three blocks (10, 11, 12) seem to form a distinct block. This seems to indicate that most of the function/task fitting occurs at these later blocks.

The presence of block structures in the GW-distance matrices indicates major functional changes may concentrate at these transition blocks. This finding may suggest that for other downstream tasks, we may consider freezing the model up to Block 8 and only fine-tuning the blocks after that. We validate this observation in appendix G. We also consider a model compression application where only 4 transformer blocks can achieve similarly good performance, as discussed in Appendix L.

When sparsifying these models, we observe the more sparse models have lesser differences among the blocks (with 95% sparse model in 6e having the least differences). This is expected as fewer parameters contribute to the final function output besides others being suppressed. Nonetheless, a similar pattern persists, indicating that later blocks differ significantly from earlier ones. This observation is consistent with fine-tuning and sparsification literature (Li et al., 2021; Dhurandhar et al., 2024), where it has been observed that later blocks typically undergo substantial changes during fine-tuning as they focus on task-specific solutions, while the earlier middle blocks remain stable as they capture syntactic and semantic patterns of the language necessary for various tasks. In

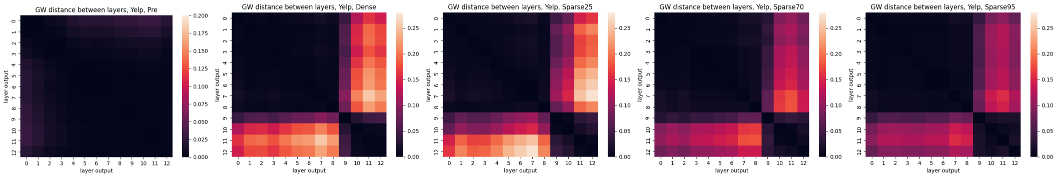

(a) Pre-trained (b) Dense (c) 25% Sparse (d) 70% Sparse (e) 95% Sparse

Figure 6: Pairwise (layer) distances on Yelp, across different BERT models, using the proposed GW distance, from top to bottom. Different columns: first column is the pre-trained BERT and the rest are fine tuned BERT models with increasing sparsity (dense, 25%, 70% and 95% sparsity). As can be seen GW clearly demarcates the (functional) sub-network blocks. Due to page limit, we show baseline results in Appendix I.

appendix J, we further investigate the GW distance between blocks from different models, providing insights into how representations vary across architectures. In Appendix I, we include results from baseline similarity measures. Overall, CKA produces also similar block structures to the proposed GW distance, though with greater variability within block structures. In contrast, other baselines fail to reveal such clear block structures.

On SST2 dataset, we also observe very similar patterns with the GW distance and 3 baselines, for which we refer the readers to appendix K for detailed results. In both datasets, low distance measure are consistently observed in the diagonal elements, but the overall block structures are not as obvious in the baselines as they are with GW distance, highlighting the effectiveness of the GW distance.

**Clustering** Besides visualization above, one can also utilize clustering methods to automatically identify the subnetworks from the GW distance. We tested spectral clustering (Von Luxburg, 2007) on a similarity matrix computed as the reverse pairwise GW distance matrix. This method successfully identified 2 groups with block $1 \sim 8$ and block $9 \sim 12$.

### 5.3 Emergence of Subnetworks During Training

We also visualize the GW distance between blocks while fine-tuning the pretrained BERT model on YELP datasets in the entire training process, in order to observe when these subnetwork structures begin to emerge. Figure 7 show a few visualization on GW distances at selected training iterations. Block distances are low in the beginning (observed in Figure 6a), but by iteration 300 the last block begin to differ from other blocks. As training progresses, block 9, 10, and 11 begin to show at iteration 3k and 15k. These growing differences in GW distance reflect the model's increasing F1 score on the test data. Overall it show the gradual specialization of blocks into distinct sub-networks, with each sub-network potentially focusing on different aspects of the task.

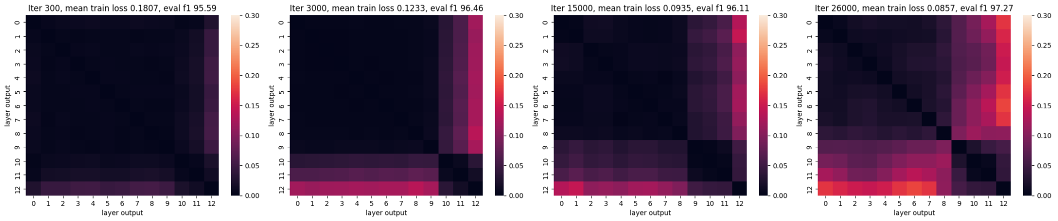

(a) Iteration = 300 (b) Iteration = 3k (c) Iteration = 15k (d) Iteration = 26k

Figure 7: Pairwise GW distance in YELP datasets, over training iterations.

We also plot the mean GW distance of all block pairs in Figure 8. Figure 8a show the mean GW distance over training iterations, and show it grows over time. Figure 8b shows that mean GW distance versus two different accuracy metric on the test dataset. GW distance grow slowly at first, followed by a rapid increase as the model achieves better accuracy and F1 scores. Such observation is consistent with existing "grokking" behavior, where validation accuracy can suddenly increases well after achieving near perfect training accuracy (Nanda et al., 2023). Similarly, Figure 8c shows a rapid increase in mean GW distance in order to achieve a lower training loss.

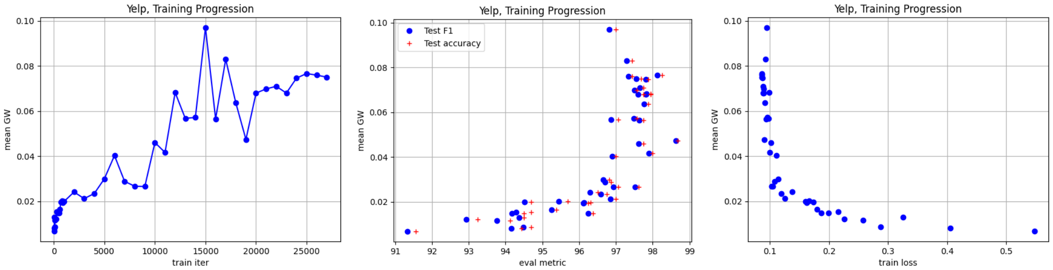

Figure 8: Pairwise GW distance in YELP datasets, over training iterations.

### 5.4 ResNet and Computer Vision Dataset

In addition to the attention-based architectures, we also test our approach on ResNet9, a popular convolutional neural network architecture(He et al., 2016; Park et al., 2023). We compare a randomly initialized ResNet9 and a trained model on CIFAR 10 image dataset CIFAR-10 (Krizhevsky et al., 2009), achieving 91.63% accuracy on the test data. For more details on the setup, we refer the readers to Appendix N. In Figure 20, we show the pairwise distance among layers using baselines that handle different input dimensions. Overall, GW distance show the most clear divisions of subnetworks.

To further examine how the sub-network structures align with learned representation, we visualize the computed distances alongside the learned representations of a ”ship” image across all layers in Figure 9. The top row shows the representations of a ship at each layer. To see the gradual changes over layers, we visualize the distance between every layer and its previous layer, using various methods capable of handling different dimensions between compared spaces. Overall, RSM, RSA, MSID, and CKA show indicate significant changes across many layers, without clear evidence of sub-network structures. AGW highlights the changes in the final few layers only. In comparison, GW distance demonstrates the most consistency with the image representations visually. Specifically, the 3rd convolution layer (Layer ID 2.ReLU) introduces the first notable differences, where the ship’s shape becomes less distinct, signaling the learning of mid-level features. The shapes become increasingly blurred in the 5th convolution layers (Layer ID 4.Conv2d ) and by Layer 4.ReLU the ship’s shape is nearly absent. The final convolutional layer (Layer ID 7.Conv2d) shows significant changes from its preceding layer (Layer ID 6.ReLU), marking the point where class-specific information is consolidated. These results suggest that GW distance aligns most effectively with the learned image representations, providing strong evidence that it can reveal meaningful subnetwork structures.

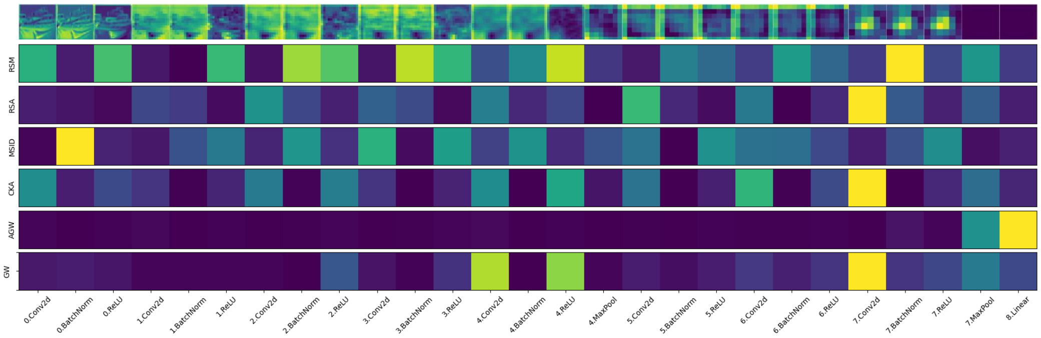

Figure 9: Pairwise layer distance between every layer and its previous layer on CIFAR-10, for various baselines.

## 6 Discussion

We proposed a novel approach to model interpretation based on functional similarity within intermediate layers of neural networks, using Gromov-Wasserstein (GW) distance to compute such similarities. To the best of our knowledge, our application of GW distance in this context is novel. On algebraic, real NLP, and vision tasks, we identified the existence of major sub-components amongst layers, corresponding to functionally meaningful abstractions. Overall, our method provides an automatic low-cost approach to find sub-components within neural networks, facilitating human understanding. Future work could investigate larger models to observe general trends and applications of functional similarity. Theoretical study of other properties of GW distances within the context of neural network interpretability is also an interesting future direction.

## REFERENCES

Adithya Bhaskar, Dan Friedman, and Danqi Chen. The heuristic core: Understanding subnetwork generalization in pretrained language models. *arXiv preprint arXiv:2403.03942*, 2024.

Nicolas Bonneel, Michiel Van De Panne, Sylvain Paris, and Wolfgang Heidrich. Displacement interpolation using lagrangian mass transport. In *Proceedings of the 2011 SIGGRAPH Asia conference*, pp. 1–12, 2011.

Trenton Bricken, Adly Templeton, Joshua Batson, Brian Chen, Adam Jermyn, Tom Conerly, Nick Turner, Cem Anil, Carson Denison, Amanda Askell, Robert Lasenby, Yifan Wu, Shauna Kravec, Nicholas Schiefer, Tim Maxwell, Nicholas Joseph, Zac Hatfield-Dodds, Alex Tamkin, Karina Nguyen, Brayden McLean, Josiah E Burke, Tristan Hume, Shan Carter, Tom Henighan, and Christopher Olah. Towards monosemanticity: Decomposing language models with dictionary learning. *Transformer Circuits Thread*, 2023. https://transformer-circuits.pub/2023/monosemantic-features/index.html.

Jiezhang Cao, Jincheng Li, Xiping Hu, Xiangmiao Wu, and Mingkui Tan. Towards interpreting deep neural networks via layer behavior understanding. *Machine Learning*, 111(3):1159–1179, 2022.

Francois Charton. Learning the greatest common divisor: explaining transformer predictions. In *The Twelfth International Conference on Learning Representations*, 2023.

Arthur Conmy, Augustine Mavor-Parker, Aengus Lynch, Stefan Heimersheim, and Adrià Garriga-Alonso. Towards automated circuit discovery for mechanistic interpretability. *Advances in Neural Information Processing Systems*, 36, 2024.

Pinar Demetci, Quang Huy Tran, Ievgen Redko, and Ritambhara Singh. Revisiting invariances and introducing priors in gromov-wasserstein distances. *arXiv preprint arXiv:2307.10093*, 2023a.

Pinar Demetci, Quang Huy Tran, Ievgen Redko, and Ritambhara Singh. Revisiting invariances and introducing priors in gromov-wasserstein distances. *arXiv:2307.10093*, 2023b.

Jacob Devlin, Ming-Wei Chang, Kenton Lee, and Kristina Toutanova. BERT: Pre-training of deep bidirectional transformers for language understanding. In Jill Burstein, Christy Doran, and Thamar Solorio (eds.), *Proceedings of the 2019 Conference of the North American Chapter of the Association for Computational Linguistics: Human Language Technologies, Volume 1 (Long and Short Papers)*, pp. 4171–4186, Minneapolis, Minnesota, June 2019. Association for Computational Linguistics. doi: 10.18653/v1/N19-1423. URL `https://aclanthology.org/N19-1423`.

Amit Dhurandhar, Tejaswini Pedapati, Ronny Luss, Soham Dan, Aurelie Lozano, Payel Das, and Georgios Kollias. Neuroprune: A neuro-inspired topological sparse training algorithm for large language models. *Findings of the Association for Computational Linguistics*, 2024.

Frances Ding, Jean-Stanislas Denain, and Jacob Steinhardt. Grounding representation similarity with statistical testing. *arXiv preprint arXiv:2108.01661*, 2021.

Maximilian Dreyer, Erblina Purelku, Johanna Vielhaben, Wojciech Samek, and Sebastian Lapuschkin. Pure: Turning polysemantic neurons into pure features by identifying relevant circuits. *arXiv preprint arXiv:2404.06453*, 2024.

Kshitij Dwivedi and Gemma Roig. Representation similarity analysis for efficient task taxonomy & transfer learning. In *Proceedings of the IEEE/CVF Conference on Computer Vision and Pattern Recognition*, pp. 12387–12396, 2019.

Rémi Flamary, Nicolas Courty, Alexandre Gramfort, Mokhtar Z. Alaya, Aurélie Boisbunon, Stanislas Chambon, Laetitia Chapel, Adrien Corenflos, Kilian Fatras, Nemo Fournier, Léo Gautheron, Nathalie T.H. Gayraud, Hicham Janati, Alain Rakotomamonjy, Ievgen Redko, Antoine Rolet, Antony Schutz, Vivien Seguy, Danica J. Sutherland, Romain Tavenard, Alexander Tong, and Titouan Vayer. Pot: Python optimal transport. *Journal of Machine Learning Research*, 22(78):1–8, 2021. URL `http://jmlr.org/papers/v22/20-451.html`.

Mor Geva, Jasmijn Bastings, Katja Filippova, and Amir Globerson. Dissecting recall of factual associations in auto-regressive language models. *arXiv preprint arXiv:2304.14767*, 2023.

Ian Goodfellow, Yoshua Bengio, and Aaron Courville. *Deep learning*. MIT press, 2016.

Kaiming He, Xiangyu Zhang, Shaoqing Ren, and Jian Sun. Deep residual learning for image recognition. In *Proceedings of the IEEE conference on computer vision and pattern recognition*, pp. 770–778, 2016.

Evan Hernandez, Arnab Sen Sharma, Tal Haklay, Kevin Meng, Martin Wattenberg, Jacob Andreas, Yonatan Belinkov, and David Bau. Linearity of relation decoding in transformer language models. *arXiv preprint arXiv:2308.09124*, 2023.

Yifan Hou, Jiaoda Li, Yu Fei, Alessandro Stolfo, Wangchunshu Zhou, Guangtao Zeng, Antoine Bosselut, and Mrinmaya Sachan. Towards a mechanistic interpretation of multi-step reasoning capabilities of language models. *arXiv preprint arXiv:2310.14491*, 2023.

Jing Huang, Zhengxuan Wu, Christopher Potts, Mor Geva, and Atticus Geiger. Ravel: Evaluating interpretability methods on disentangling language model representations. *arXiv preprint arXiv:2402.17700*, 2024a.

Xinting Huang, Madhur Panwar, Navin Goyal, and Michael Hahn. Inversionview: A general-purpose method for reading information from neural activations. *arXiv preprint arXiv:2405.17653*, 2024b.

Max Klabunde, Tobias Schumacher, Markus Strohmaier, and Florian Lemmerich. Similarity of neural network models: A survey of functional and representational measures. *arXiv preprint arXiv:2305.06329*, 2023.

Simon Kornblith, Mohammad Norouzi, Honglak Lee, and Geoffrey Hinton. Similarity of neural network representations revisited. In *International conference on machine learning*, pp. 3519–3529. PMLR, 2019.

János Kramár, Tom Lieberum, Rohin Shah, and Neel Nanda. Atp*: An efficient and scalable method for localizing llm behaviour to components. *arXiv preprint arXiv:2403.00745*, 2024.

Alex Krizhevsky, Geoffrey Hinton, et al. Learning multiple layers of features from tiny images. 2009.

Jiaoda Li, Ryan Cotterell, and Mrinmaya Sachan. Differentiable subset pruning of transformer heads. *Trans. Assoc. Comput. Linguistics*, 9:1442–1459, 2021. doi: 10.1162/TACL_A_00436. URL `https://doi.org/10.1162/tacl_a_00436`.

Yixuan Li, Jason Yosinski, Jeff Clune, Hod Lipson, and John Hopcroft. Convergent learning: Do different neural networks learn the same representations? *arXiv preprint arXiv:1511.07543*, 2015.

Suhas Lohit and Michael Jones. Model compression using optimal transport. In *Proceedings of the IEEE/CVF Winter Conference on Applications of Computer Vision*, pp. 2764–2773, 2022.

Ilya Loshchilov and Frank Hutter. Decoupled weight decay regularization. *arXiv preprint arXiv:1711.05101*, 2017.

Johannes Mehrer, Courtney J Spoerer, Nikolaus Kriegeskorte, and Tim C Kietzmann. Individual differences among deep neural network models. *Nature communications*, 11(1):5725, 2020.

Facundo Mémoli. Gromov–wasserstein distances and the metric approach to object matching. *Foundations of computational mathematics*, 11:417–487, 2011.

Kevin Meng, David Bau, Alex Andonian, and Yonatan Belinkov. Locating and editing factual associations in gpt. *Advances in Neural Information Processing Systems*, 35:17359–17372, 2022.

Ari Morcos, Maithra Raghu, and Samy Bengio. Insights on representational similarity in neural networks with canonical correlation. *Advances in neural information processing systems*, 31, 2018.

Neel Nanda, Lawrence Chan, Tom Lieberum, Jess Smith, and Jacob Steinhardt. Progress measures for grokking via mechanistic interpretability. *arXiv preprint arXiv:2301.05217*, 2023.

Thao Nguyen, Maithra Raghu, and Simon Kornblith. On the origins of the block structure phenomenon in neural network representations. *arXiv preprint arXiv:2202.07184*, 2022.

Francesco Ortu, Zhijing Jin, Diego Doimo, Mrinmaya Sachan, Alberto Cazzaniga, and Bernhard Schölkopf. Competition of mechanisms: Tracing how language models handle facts and counterfactuals. *arXiv preprint arXiv:2402.11655*, 2024.

Vedant Palit, Rohan Pandey, Aryaman Arora, and Paul Pu Liang. Towards vision-language mechanistic interpretability: A causal tracing tool for blip. In *Proceedings of the IEEE/CVF International Conference on Computer Vision*, pp. 2856–2861, 2023.

Kiho Park, Yo Joong Choe, Yibo Jiang, and Victor Veitch. The geometry of categorical and hierarchical concepts in large language models. *arXiv preprint arXiv:2406.01506*, 2024.

Sung Min Park, Kristian Georgiev, Andrew Ilyas, Guillaume Leclerc, and Aleksander Madry. Trak: Attributing model behavior at scale. *arXiv preprint arXiv:2303.14186*, 2023.

Gabriel Peyré, Marco Cuturi, et al. Computational optimal transport: With applications to data science. *Foundations and Trends® in Machine Learning*, 11(5-6):355–607, 2019.

Claudia Shi, Nicolas Beltran-Velez, Achille Nazaret, Carolina Zheng, Adrià Garriga-Alonso, Andrew Jesson, Maggie Makar, and David Blei. Hypothesis testing the circuit hypothesis in llms. In *ICML 2024 Workshop on Mechanistic Interpretability*, 2024.

Sidak Pal Singh and Martin Jaggi. Model fusion via optimal transport. *Advances in Neural Information Processing Systems*, 33:22045–22055, 2020.

George Stoica, Daniel Bolya, Jakob Bjorner, Pratik Ramesh, Taylor Hearn, and Judy Hoffman. Zipit! merging models from different tasks without training. *arXiv preprint arXiv:2305.03053*, 2023.

Vayer Titouan, Nicolas Courty, Romain Tavenard, and Rémi Flamary. Optimal transport for structured data with application on graphs. In *International Conference on Machine Learning*, pp. 6275–6284. PMLR, 2019.

Anton Tsitsulin, Marina Munkhoeva, Davide Mottin, Panagiotis Karras, Alex Bronstein, Ivan Oseledets, and Emmanuel Müller. The shape of data: Intrinsic distance for data distributions. *arXiv preprint arXiv:1905.11141*, 2019.

Laurens Van der Maaten and Geoffrey Hinton. Visualizing data using t-sne. *Journal of machine learning research*, 9(11), 2008.

Ashish Vaswani, Noam Shazeer, Niki Parmar, Jakob Uszkoreit, Llion Jones, Aidan N Gomez, Łukasz Kaiser, and Illia Polosukhin. Attention is all you need. *Advances in neural information processing systems*, 30, 2017.

Ulrike Von Luxburg. A tutorial on spectral clustering. *Statistics and computing*, 17:395–416, 2007.

Alex Wang, Amanpreet Singh, Julian Michael, Felix Hill, Omer Levy, and Samuel R. Bowman. Glue: A multi-task benchmark and analysis platform for natural language understanding. In *Proceedings of the 24th International Conference on Learning Representations*, 2019.

Kevin Wang, Alexandre Variengien, Arthur Conmy, Buck Shlegeris, and Jacob Steinhardt. Interpretability in the wild: a circuit for indirect object identification in gpt-2 small. *arXiv preprint arXiv:2211.00593*, 2022.

Lei Yu, Meng Cao, Jackie Chi Kit Cheung, and Yue Dong. Mechanisms of non-factual hallucinations in language models. *arXiv preprint arXiv:2403.18167*, 2024.

Lei Zheng, Yang Xiao, and Lingfeng Niu. A brief survey on computational gromov-wasserstein distance. *Procedia Computer Science*, 199:697–702, 2022. ISSN 1877-0509. doi: https://doi.org/10.1016/j.procs.2022.01.086. The 8th International Conference on Information Technology and Quantitative Management (ITQM 2020 & 2021): Developing Global Digital Economy after COVID-19.

Ziqian Zhong, Ziming Liu, Max Tegmark, and Jacob Andreas. The clock and the pizza: Two stories in mechanistic explanation of neural networks. *Advances in Neural Information Processing Systems*, 36, 2024.

# A Representations in Transformer-based and Convolution Neural Network

We consider multiple candidate $Y$'s to form the search space for target $Y^0$. In the context of MLP neural networks for example, where $\sigma(.)$ denotes the non-linearity and $W$s are the parameter matrices, we have $Y^* = W_n(\sigma(W_{n-1} \dots \sigma(W_1 X)))$ for the whole network. We can extract many $Y$'s from intermediate functions of the model, for instance $Y_1 = W_1 X$, $Y_2 = \sigma(W_1 X)$, and so on. These $Y$'s are often called representations, activations, or sometimes even "outputs" from each layer.

For attention modules in transformer neural networks (Vaswani et al., 2017), we can similarly extract $Y$'s from attention key, query, and value functions as well as MLP functions. More specifically, a deep transformer architecture of depth $l$ is formed by sequentially stacking $l$ transformer blocks. Each transformer block takes the representations of a sequence $\boldsymbol{X}_{\text{in}} \in \mathbb{R}^{T \times d}$, where $\boldsymbol{X}_{\text{in}}$ = Emb$(\boldsymbol{X})$ with embedding layer Emb and input $\boldsymbol{X}$, $T$ is the number of tokens and $d$ is the embedding dimension, and outputs $\boldsymbol{X}_{\text{out}}$, where:

$$\begin{aligned} \boldsymbol{X}_{\text{out}} &= \alpha_{\text{FF}} \hat{\boldsymbol{X}} + \beta_{\text{FF}} \text{MLP}(\text{Norm}(\hat{\boldsymbol{X}})) \\ \text{where,} \quad \text{MLP}(\boldsymbol{X}_m) &= \sigma(\boldsymbol{X}_m \boldsymbol{W}^1) \boldsymbol{W}^2 \\ \hat{\boldsymbol{X}} &= \alpha_{\text{SA}} \boldsymbol{X}_{\text{in}} + \beta_{\text{SA}} \text{MHA}(\text{Norm}(\boldsymbol{X}_{\text{in}})), \\ \text{MHA}(\boldsymbol{X}) &= [\text{Attn}_1(\boldsymbol{X}), \dots, \text{Attn}_H(\boldsymbol{X})] \boldsymbol{W}^P, \\ \text{Attn}(\boldsymbol{X}) &= \boldsymbol{A}(\boldsymbol{X}) \boldsymbol{X} \boldsymbol{W}^V, \\ \boldsymbol{A}(\boldsymbol{X}) &= \text{softmax}\left( \frac{1}{\sqrt{d_k}} \boldsymbol{X} \boldsymbol{W}^Q \boldsymbol{W}^{K^\top} \boldsymbol{X}^\top + \boldsymbol{M} \right), \end{aligned} \tag{2}$$

with scalar weights $\alpha_{\text{FF}}$, $\beta_{\text{FF}}$ , $\alpha_{\text{SA}}$, and $\beta_{\text{SA}}$ usually set to 1 by default. Here FF stands for feedforward network, SA stands for self-attention, MHA is Multi-Head Attention, and Norm is a normalization layer. MLP usually has a single hidden layer with dimension $d$ and ReLU activation. The MHA sub-block shares information among tokens by using self-attention with $\boldsymbol{W}^Q$, $\boldsymbol{W}^K$ and $\boldsymbol{W}^V$ indicating query, key and value matrices. We list the exact locations of representations considered in the transformer models in Table 2.

Table 2: Representations $Y$ in the attention-based model considered in experiments as per equation 2. Omitting $Y$ in most names for readability.

| | | | | | | |
|---|---|---|---|---|---|---|
| (Across Blocks) | | | | | | |
| Name | Resid-Pre$^l$ | $Y^l$, at each block | | | | |
| Value | $= \boldsymbol{X}_{\text{in}}^l$ | $= \boldsymbol{X}_{\text{out}}^l$ | | | | |
| (Within Each Block $l$) | | | | | | |
| Name | Attn-Out$^l$ | Resid-Mid$^l$ | Pre | Post | MLP-out$^l$ | Resid-Post$^l$ |
| Value | =MHA$(\boldsymbol{X})^l$ | $= \hat{\boldsymbol{X}}$ | $= \hat{\boldsymbol{X}} \boldsymbol{W}^1$ | =MLP$(\hat{\boldsymbol{X}})$ | = MLP$(\hat{\boldsymbol{X}})$ | $= \boldsymbol{X}_{\text{out}}$ |
| (Within Each Attention Head $h$) | | | | | | |
| Name | $k_h$ | $q_h$ | Attn-Pre$_h$ | Attn$_h$ | v$_h$ | z$_h$ |
| Value | $= \boldsymbol{X}\boldsymbol{W}^K$ | $= \boldsymbol{X}\boldsymbol{W}^Q$ | $= q_h k_h^T$ | $= \boldsymbol{A}(\boldsymbol{X})$ | $= \boldsymbol{X}\boldsymbol{W}^V$ | =Attn$(\boldsymbol{X})$ |

We also consider convolution neural networks for computer vision datasets. Specifically, we use a relatively lightweight ResNet9 (He et al., 2016; Park et al., 2023). The exact locations of the candidate representations considered are listed in Table 3.

# B Modular Sum Experiment Details

We use the same architecture and protocols in training, as previous modular papers (Nanda et al., 2023; Zhong et al., 2024), based on their available Github repos. Specifically, we use transformer width $d = 128$, and each attention head has 32 dimensions. As a result, MLP has 512 hidden neurons. ReLU is used as the activation throughout the models,

Table 3: All representations $Y$ considered in ResNet 9 in experiments.

| | | | | |
|---|---|---|---|---|
| (Module 0) | | | | |
| Name | 0.Conv2d | 0.BatchNorm | 0.ReLU | |
| Details | in-channel = 3, out =64, kernel size = (3,3) | Batch Normalization | activation | |
| (Module 1) | | | | |
| Name | 1.Conv2d | 1.BatchNorm | 1.ReLU | |
| Details | in-channel = 64, out =128, kernel size = (5,5) | Batch Normalization | activation | |
| (Module 2 & 3: Residual Block ) | | | | |
| Name | 2.Conv2d | 2.BatchNorm | 2.ReLU | |
| Name | 3.Conv2d | 3.BatchNorm | 3.ReLU | |
| Details | in-channel = 128, out =128, kernel size = (3,3) | Batch Normalization | activation | |
| (Module 4) | | | | |
| Name | 4.Conv2d | 4.BatchNorm | 4.ReLU | 4. MaxPool |
| Details | in-channel = 128, out =256, kernel size = (3,3) | Batch Normalization | activation | Kernel (2,2) |
| (Module 5 & 6: Residual Block ) | | | | |
| Name | 5.Conv2d | 5.BatchNorm | 5.ReLU | |
| Name | 6.Conv2d | 6.BatchNorm | 6.ReLU | |
| Details | in-channel = 256, out =256, kernel size = (3,3) | Batch Normalization | | |
| (Module 7) | | | | |
| Name | 7.Conv2d | 7.BatchNorm | 7.ReLU | 7. MaxPool |
| Details | in-channel = 256, out =128, kernel size = (3,3) | Batch Normalization | activation | Adaptive |
| (Module 8) | | | | |
| Name | 8.Linear (classification) | | | |
| Details | in-feature = 128, out =10 | | | |

**Data** Among all data points ($59^2 = 3481$ of them), we randomly select 80% as training samples and 20% as validation samples.

**Hyperparameters** We used AdamW optimizer (Loshchilov & Hutter, 2017) with learning rate $\gamma = 0.001$ and weight decay factor $\beta = 2$. We use the shuffled data as one batch in every epoch. We train models from scratch and train for 26,000 epoches.

**Search Space** For the $f_{\text{mod3}}$ dataset, we consider all layers in the network, including all representations within transformer blocks. As shown in Table 2, each attention head has 6 intermediate layers, for a total of 24. Each block has an additional 7 layers (1 input layer, Resid-Pre, and 6 intermediate layers). Hence, for three blocks each with four attention heads, we have a total of 93 representations to evaluate, as each block has $31 = 24 + 7$ representations.

## C Probes on Modular Sum Dataset: When Target is Known

When the target is a value from a known function, we can directly compare outputs between representations from each layer and the known function output. Representations from each layer can be directly compared with the target via a probe. We first consider **Model E** and then **Model L**.

**Linear Probe** Popular linear probes can be used to assess the similarity between a target and any layer's representation. We perform linear regression of each target $(c_1, c_2, c)$ on each of the 93 representations $Y$, and report the residual error as the scoring distance function between $Y$ and $c$'s.

**Results** Since we perform layer-wise training with **Model L**, we know the true locations of $c_1$ and $c_2$, which sit at $\boldsymbol{X}_{\text{out}}^1$ and $\boldsymbol{X}_{\text{out}}^2$ with names Resid-Post$^1$ and Resid-Post$^2$, respectively. As shown in the top part of Table 4, a linear regression probe can predict targets perfectly with these two layers. In fact, there are 21 other layers which also show perfect accuracy. For $c_1$, these consist of Post$^0$ and MLP-out$^0$ from the same block and some layers from the next block, including linear operations with all $k$'s, $q$'s, $v$'s. The final prediction $c$ can be linearly predicted as expected, due to the model's perfect prediction accuracy.

Table 4: Linear and Nonlinear Probe Results, for $f_{\text{mod3}}$ dataset.

| Model L | Linear Probe for | Perfect Match? | Top Similar Layers | $D_{\text{min}} =$ |
|---|---|---|---|---|
| | $c_1$ | ✓ | Resid-Post$^1$ and 21 others | 0 |
| | $c_2$ | ✓ | Resid-Post$^2$ and 21 others | 0 |
| | $c$ | ✓ | Resid-Post$^3$ and Post$^2$ | 0 |
| **Model E** | **Linear Probe for** | **Perfect Match?** | **Top Similar Layers** | $D_{\text{min}} =$ |
| | $c_1$ | × | Post$^2$ | 0.522 |
| | $c_2$ | × | Post$^1$ | 0.93 |
| | $c$ | ✓ | Resid-Post$^3$ and 5 others | 0 |
| **Model E** | **Nonlinear Probe for** | **Perfect Match?** | **Top Similar Layers** | $D_{\text{min}} =$ |
| | $c_1$ | ✓ | Resid-Post$^1$ and 15 others | 0 |
| | $c_2$ | ✓ | Resid-Post$^1$ and 4 others | 0 |
| | $c$ | ✓ | Resid-Post$^3$ and 9 others | 0 |

Naturally we would like to confirm if the same happens with **Model E**: if we use the same linear probe, does each block in **Model E** learn the corresponding $c$ at the output of the transformer block? As shown in the mid part of Table 4, we are not able to find any layer that produces a representation that is linearly predictive of $c_1$ and $c_2$, with the lowest prediction errors at $52\%$ and $93\%$, respectively. Moreover, the most similar layers to $c_1$ and $c_2$ are in the 2nd block and 1st block respectively, instead of the expected 1st and 2nd blocks. This seems to suggest that **Model E** does not actually learn any function of $c_1$ and $c_2$.

**Non-linear Probe** As discussed previously, to deal with the potentially large search space of functions of the target, a more powerful probe (such as a nonlinear MLP function) may have to be used so that it can detect more complex similarities to $c$. Therefore, we train a two-layer MLP[2] to predict $c$'s. As shown at the bottom of Table 4, these two-layer MLPs have more predictive power and can perfectly predict the targets, while still showing differences among various layers indicating that the matched layers do capture the intended target functions while other layers do not. Many layers in the 3rd block, for example, have only $1\%$ accuracy relative to $c_1$. This indicates that non-linear probes can be used to find subgroups of layers in neural networks. Unlike existing work that primarily focuses on linear probes, we show that non-linear probes, still with limited capacity, are useful.

One issue with using predictive probes to compute the distance measure $D$ is that the target function has to be known. In practice, however, we may not know any intermediate targets, as suggested in the end-to-end training of **Model E**. While we still can try different target functions and use non-linear probes, the infinite number of possible targets makes such an approach inefficient. This calls for a different strategy to differentiate sub-components in a network through representation similarity.

## D Baseline Comparison Results on Modular Sum

We have also tested a few baselines that can handle different space dimensions, shown in Figure 10. RSA and CKA reveal different levels of subnetworks within attention layers and across transformer blocks. AGW demonstrates the highest sensitivity to attention computations, while RSM finds the last few layers within each transformer block.

## E Real NLP Experiment Details

We analyze a BERT-base-uncased (Devlin et al., 2019) model based on our optimal matching inspired mechanistic interpretability approach. We fine tune it on two well known datasets in NLP; i) Yelp reviews (`https://www.kaggle.com/code/suzanaiacob/sentiment-analysis-of-the-yelp-reviews-data`) and ii) Stanford Sentiment Treebank-v2 (SST2), which is part of the GLUE NLP benchmark (Wang et al., 2019). Both of these are sentiment analysis tasks, where the goal is to predict if a piece of text has positive or

[2] We use the neural network classifier from the scikit-learn package, with default parameters.

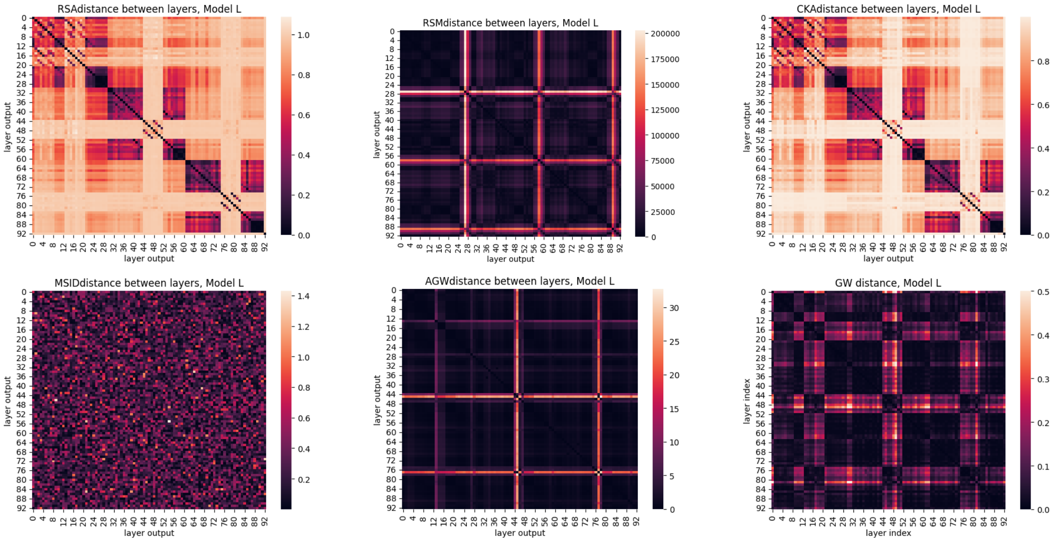

Figure 10: Pairwise (layer) distances on Modular Sum dataset, with layer-wise trained models. Different figures from left to right, top to bottom: *RSA, RSM, CKA, MSID, AGW, and the proposed GW distance*.

negative sentiment. The Yelp dataset has hundreds of thousands of reviews, while the SST2 dataset has tens of thousands of sentences. The training details are as follows: i) Hardware: $1$ A100 Nvidia GPU and $1$ intel CPU, ii) Max. Sequence Length : $256$, iii) Epochs: $1$, iv) Batch Size: $16$ and v) Learning Rate: $2e^{-5}$ with no weight decay. The accuracy on Yelp was $97.87\%$, while that on SST2 was $92.4\%$. Without fine tuning the pre-trained BERT models accuracy on Yelp and SST2 was $49.29\%$ and $50.34\%$ respectively indicative of random chance performance.

We also fine tuned a series of sparse models on these datasets. The method we used to sparsify was a state-of-the-art dynamic sparse training approach NeuroPrune (Dhurandhar et al., 2024), which leads to high performing structured sparse models. Using this approach and the same training settings as above we created BERT models with $25\%$, $70\%$ and $95\%$ sparsity which had accuracies of $96.31\%$, $97.53\%$ and $96.22\%$ respectively for the Yelp dataset and accuracies of $90.25\%$, $88.5\%$ and $84.4\%$ respectively for the SST2 dataset. We then used the resultant models for our analysis.

## F Alignment from GW distance

We plot a tSNE projection (Van der Maaten & Hinton, 2008) down to 2 dimensions, on a batch of 16 samples (color indicative of sample) on YELP, and visualize it in Figure 11e. As one can see, the sample neighborhood changes across layers, which can be indicative of functional changes but something that is not captured by comparing distributions. However, GW can also account for such changes.

We also show Jaccard similarity measure on top-5-neighbors, per Euclidean distances on tSNE projection, of each of 3 samples across different transformer blocks. Jaccard similarity is a measure of two sets, computed as their intersection divided by their union. Results are shown in Table 5. This further shows the sample neighborhood changes across layers, and representation similarity measures should account for such changes.

Table 5: Jaccard Similarity on top-5-neighbors of Selected Samples across all transformer blocks.

| Sample 1<br>Block 0 v.s. | 1<br>0.25 | 2<br>0.25 | 3<br>0.25 | 4<br>0.11 | 5<br>0.43 | 6<br>0.11 | 7<br>0.25 | 8<br>0.25 | 9<br>0.11 | 10<br>0.11 | 11<br>0.25 | 12<br>0.25 | Mean<br>**0.27** |
|---|---|---|---|---|---|---|---|---|---|---|---|---|---|
| Sample 2<br>Block 0 v.s. | 1<br>0.11 | 2<br>043 | 3<br>0.11 | 4<br>0.11 | 5<br>0.11 | 6<br>0.0 | 7<br>0.11 | 8<br>0.25 | 9<br>0.25 | 10<br>0.43 | 11<br>0.25 | 12<br>0.25 | Mean<br>**0.26** |
| Sample 3<br>Block 0 v.s. | 1<br>0.0 | 2<br>0.11 | 3<br>0.43 | 4<br>0.25 | 5<br>0.25 | 6<br>0.25 | 7<br>0.11 | 8<br>0.66 | 9<br>0.11 | 10<br>0.11 | 11<br>0.11 | 12<br>0.0 | Mean<br>**0.26** |

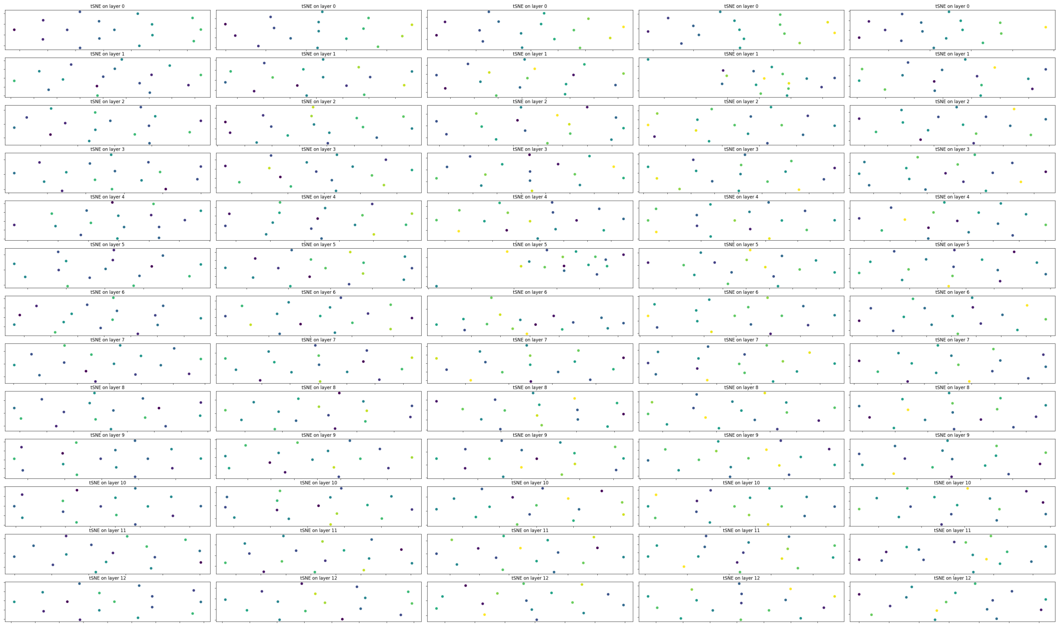

(a) Pretrained (b) Dense (c) 25% Sparse (d) 70% Sparse (e) 90% Sparse

Figure 11: tSNE projection on intermediate representations on Yelp, across BERT models with different sparsity levels. Different Rows: Results from all 12 transformer blocks, from top to bottom. Different columns: first column is the pre-trained BERT and the rest are fine tuned BERT models with increasing sparsity (dense, 25%, 70% and 95% sparsity).

To show the exact transportation plan from GW distances, we choose plot one batch of data with size 16, and show the transportation plan over 5 random layer pairs in Figure 12. As one can see, the transportation plan does not conform to identity-mapping. Both Wasserstein and Euclidean distance will likely have trouble handle in this case. We also note that the transportation plan shown Figure 12 is a permutation of the original data, rather than a distributed transportation plan. This behavior is consistent with existing Wasserstein optimal transport plan under certain conditions (Peyré et al., 2019).

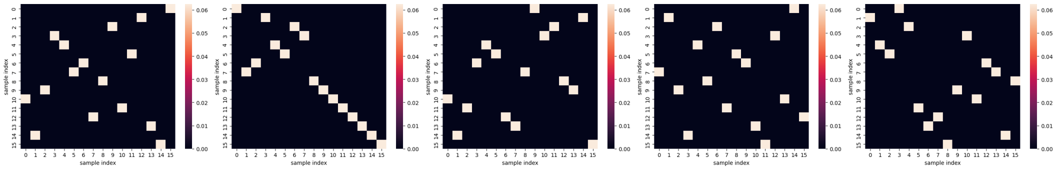

(a) (b) (c) (d) (e)

Figure 12: Pairwise GW transportation plan on Yelp, across BERT models. 5 of randomly chosen layer pairs are shown.

To complement Figure 2 on other fine-tuned BERT models on YELP, we also plot all the histograms of pairwise distances between two samples in a batch, across all layers for each of 5 models in Figure 13. Pre-trained models are publicly available models training on other datasets. Row b) to e) are the fine-tuned models on YELP, with different sparsity levels. As one can see, pretrained models do not have much differentiations across layers in the histograms, with maximal KL-divergence of 0.11 between histogram in consecutive layers. Fine tuned models, on the other hard, show larger KL-divergence values, in particular in later layers. For example, Layers 9 in the Dense BERT model contains KL distance of 1.58 from its previous layer. The results show that significant transformations in pairwise distances occur across layers and such distances would be captured by GW distances, as show in Figure 6 and Figure 15.

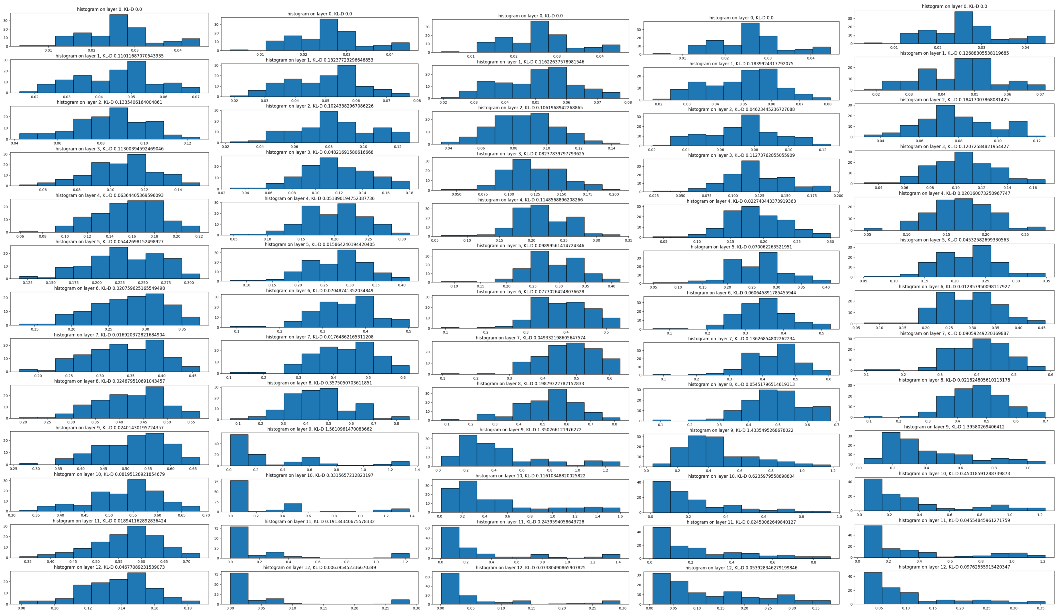

(a) Pretrained (b) Dense (c) 25% Sparse (d) 70% Sparse (e) 95% Sparse

Figure 13: Histogram on pairwise distances on Yelp, across BERT models with different sparsity levels. $a)$ is the pre-trained BERT and the rest are fine tuned BERT models with increasing sparsity levels: $(b)$densely fine-tuned, $c)$ 25%, $d)$ 70% and $e)$ 95% sparsity.

## G Fine-tuning with Different Layers

Since the GW distance indicates significant changes occurs only at later layers in YELPS, we investigate performance of fine-tuning only partial layers from pretrained models, by freezing early layers during training and training only later layers alongside a classification layer (denoted as C) at the end. In Table 6, we can see that there is no significant performance differences between fine-tuning layer 8 to 12 and fine-tuning layer 9 to 12 (0.04% drop). On the other hand, the accuracy drops 6 times more by freezing layer 1 to 9, with 0.25%. Freezing layer 1 to 10 results 0.49% drop, and finally fine-tuning only 12 results 3.59% drop. These findings validate that the later layers are crucial for significant functional changes.

Table 6: Accuracy of fine-tuning partial layers in various BERT models. C denotes the classification layer on top of BERT models.

| Fine-tune | All | 8∼12 + C | 9∼12 + C | 10∼12 + C | 11∼12 + C | Only 12 + C |
|---|---|---|---|---|---|---|
| Accuracy (%) | 97.87 | 97.47 | 97.43 | 97.19 | 96.7 | 93.11 |

## H Baseline Methods and Implementation Details

Besides the standard Euclidean and cosine distances, we compare a few other baselines, as discussed below.

Wasserstein Distance (Dwivedi & Roig, 2019): We use the POT, python optimal transport library `pythonot` (Flamary et al., 2021), with the algorithm proposed in (Bonneel et al., 2011).

Representational similarity metric (RSM) (Klabunde et al., 2023): RSM compares two different spaces by using the $L_2$ norms on differences in inter-instances distances. This can be seen as approximation to GW using the fixed and identity transportation plan (i.e., the samples map to itself). We use existing implementation at: `https://github.com/mklabunde/llm_repsim/blob/main/llmcomp/measures/rsm_norm_difference.py`.

Representational Similarity Analysis (RSA) (Klabunde et al., 2023): RSA is similar to RSM but use correlation instead of $L_2$-norm to compute the final distance. Implementation at: `https://github.com/mklabunde/llm_repsim/blob/main/llmcomp/measures/rsa.py`

Canonical Correlation analysis (CCA) (Morcos et al., 2018): CCA compute distances based on variances and covariances. Implementation at: `https://github.com/google/svcca/blob/master/cca_core.py`

Centered Kernel Alignment (CKA) (Kornblith et al., 2019): CKA is based on normalized Hilbert-Schmidt Independence Criterion (HSIC). Implementation at: `https://github.com/mklabunde/llm_repsim/blob/main/llmcomp/measures/cka.py`

Multi-Scale Intrinsic Distance (MSID) Tsitsulin et al. (2019): MSID compute the intrinsic and multiple distance, and can be considered as a lower bound of the GW distance. Implementation at: `https://github.com/xgfs/imd/blob/master/msid/msid.py`. We have explored different hyperparameter settings with different neighbors k (5 or all batch data available) and number of iterations for SLQ, but results are all similar to the default parameter setting.

Augmented GW (AGW) (Demetci et al., 2023a): AGW considers feature alignment in addition to sample alignment. Its overall objective can be seen as a penalized GW distance. Implementation at: `https://github.com/pinardemetci/AGW-AISTATS24/tree/main`.

For all methods, we use default parameter settings to obtain results in the paper. Note that RSM, RSA, CCA, MSID, and AGW, along with our proposed approach can handle different dimensions of inputs.

Gromo-Wasserstein Distance (Dwivedi & Roig, 2019): We use the POT, python optimal transport library `pythonot` (Flamary et al., 2021). We use the solver based on the conditional gradient (Titouan et al., 2019).

## I More Baselines on YELP

Due to the page limit, here we include baseline results on Yelp Datasets in Figure 14 and Figure 15.

We compare the proposed GW distance with Euclidean, Cosine, and Wasserstein distance as baselines in Figure 14, on the same YELP dataset and with the same settings. Euclidean distance between two layers' outputs, shown in the first row of Figure 14, can be seen as the GW distance with a fixed identity-mapping transportation plan for each sample. This validates the low-valued diagonal elements. Off-diagonal elements show greater variation, and it is less obvious there are two distinct sub-groups within layers. The similar pattern is also observed with Cosine and Wasserstein distances, with similar strong diagonal pattern but more pronounced block structures than Euclidean distance. we also include 6 other baseline similarity measure in Figure 15. Overall, CKA produces also similar block structures to the proposed GW distance, though with greater variability within block structures. In contrast, other baselines fail to reveal such clear block structures.

## J Cross Model Comparison

We can also use GW distance to compare layers from different BERT models. Shown in Figure 16, pretrained and densely fine-tuned BERT models exhibit different similarity measures when compared to fine-tuned BERT models with different levels of sparsity.

## K SST2 Datasets

Besides YELP Datasets, we also tested the GW distance on SST2 dataset. Results on SST2 dataset are shown in Figure 17 again confirm there exist two-three different groups in terms of functional similarity. The first major difference is seen at layers 10 and 11, while layer 12 forms its own block. When sparsifying these models, lesser differences are observed in general as also seen on the YELP dataset. Other baselines provide less clarity on the division of sub-components.

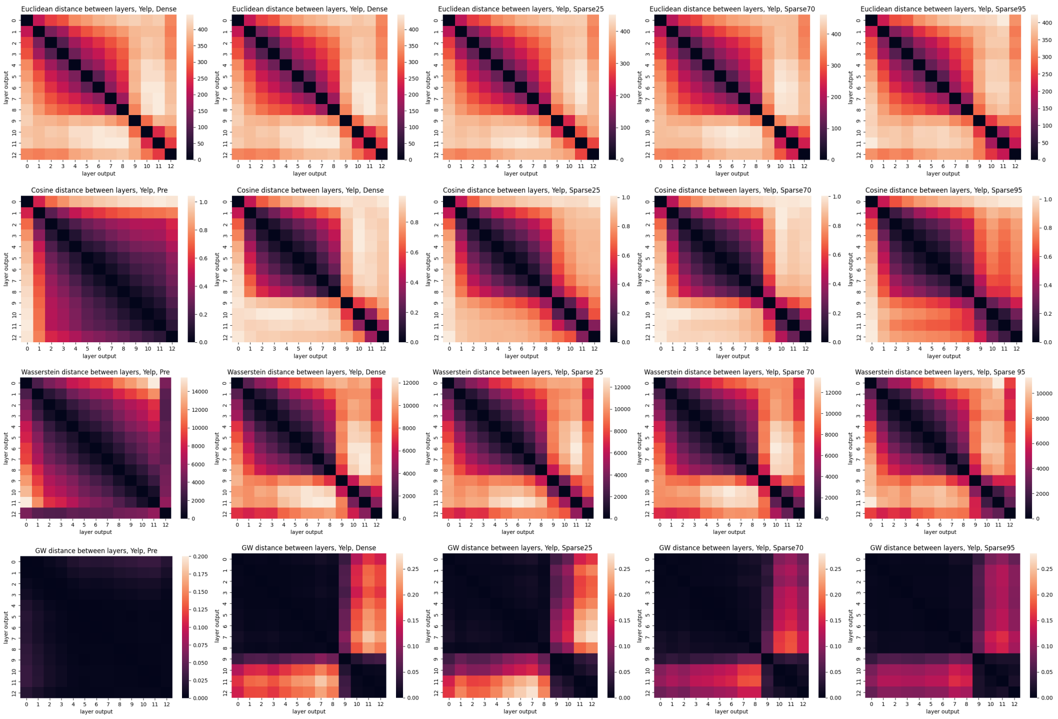

(a) Pre-trained (b) Dense (c) 25% Sparse (d) 70% Sparse (e) 95% Sparse

Figure 14: Pairwise (layer) distances on Yelp, across different BERT models. Different Rows: *Euclidean, Cosine, Wasserstein, and the proposed GW distance*, from top to bottom. Different columns: first column is the pre-trained BERT and the rest are fine tuned BERT models with increasing sparsity (dense, 25%, 70% and 95% sparsity). As can be seen GW clearly demarcates the (functional) sub-network blocks.

More baselines are included in Figure 18, as they do not all fit into the one page. Overall, RSA and CKA identify block structures but with larger 2nd block.

## L MODEL PRUNING/COMPRESSING

Another another potential application beside freezing-and-fine-tuning specific transformer blocks, we study the problem of model compress or pruning with the discovered subnetworks.

For each of desired block sizes, we take the original pre-trained BERT and only use the first $n = \{12, 8, 4, 2, 1, 0\}$ transformer blocks while discarding the rest. Note that $n = 12$ means we use all the transformer blocks, resulting the same BERT model. $n = 0$, on the other hand, means that we only use a (linear) classifier layer (after embedding layer) to predict the class label. The results are shown in Table 7. As a reminder, GW distance suggest the last 4 blocks in YELP (see Figure 6) and the last 2 blocks in SST (see Figure 17) are mostly different, which is marked by star $(*)$ in the table. It shows that by using a limited number of layers, we can achieve similar performance with the full 12 block model, with $0.01\%$ and $0.54\%$ differences in YELP and SST, respectively. Using one fewer transformer block can risk much worse reduction of performance, with $0.10\%$ and $8.60\%$ differences (about 10 times worse performance reduction).

Table 7: Accuracy of pruning BERT with a smaller number of blocks on YELP and SST. N denotes the number of transformer blocks in the new BERT models.

| Number of Transformer Blocks | 12 (all) | 8 | 4 | 2 | 1 | 0 (only classifier) |
|---|---|---|---|---|---|---|
| YELP | 97.87 | 97.87 | 97.86$^*$ | 97.76 | 97.11 | 60.3 |
| SST | 92.40 | 90.25 | 90.25 | 91.86$^*$ | 83.26 | 50.92 |

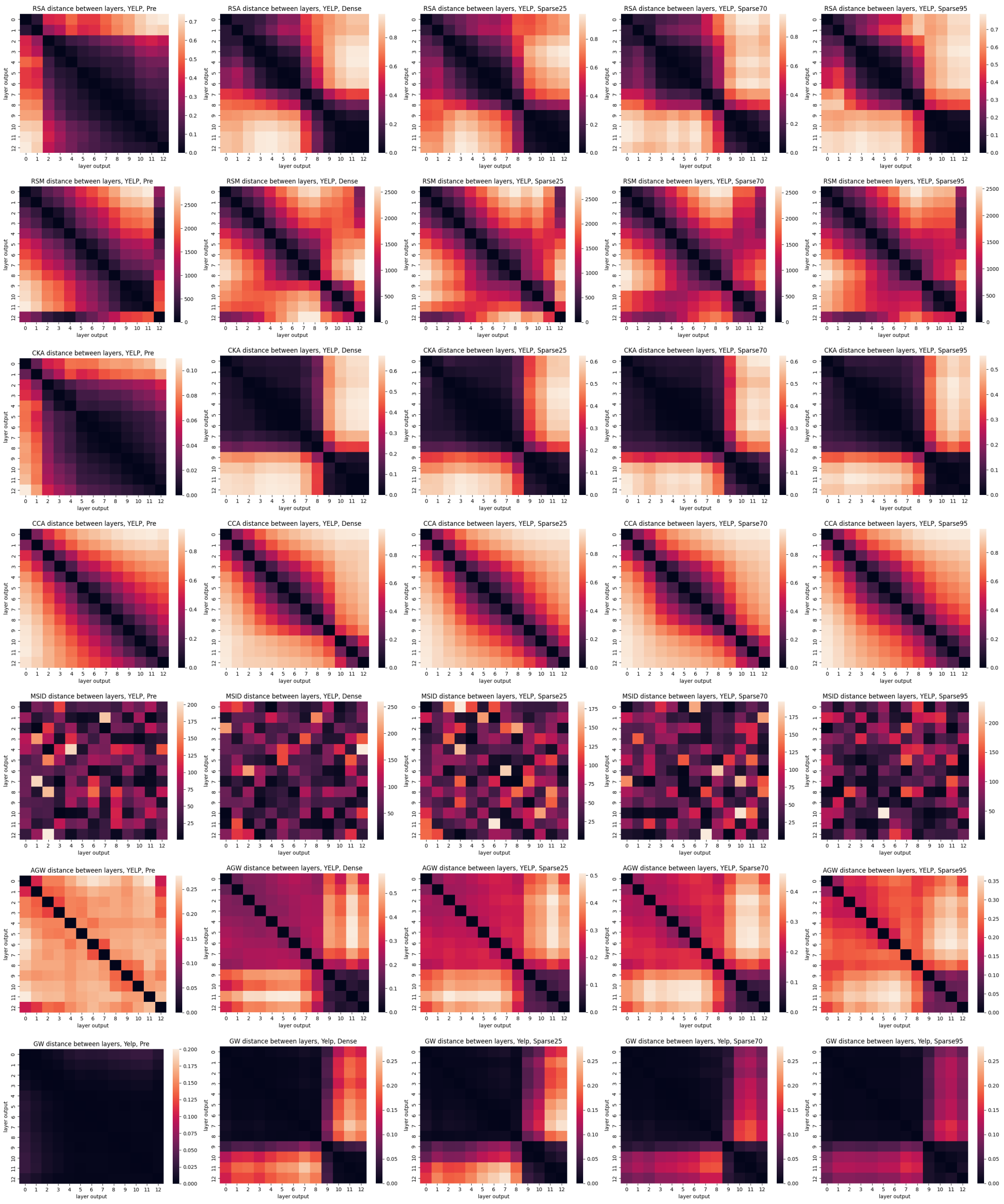
RSA distance between layers, YELP, Pre
RSA distance between layers, YELP, Dense
RSA distance between layers, YELP, Sparse25
RSA distance between layers, YELP, Sparse70
RSA distance between layers, YELP, Sparse95
RSM distance between layers, YELP, Pre
RSM distance between layers, YELP, Dense
RSM distance between layers, YELP, Sparse25
RSM distance between layers, YELP, Sparse70
RSM distance between layers, YELP, Sparse95
CKA distance between layers, YELP, Pre
CKA distance between layers, YELP, Dense
CKA distance between layers, YELP, Sparse25
CKA distance between layers, YELP, Sparse70
CKA distance between layers, YELP, Sparse95
CCA distance between layers, YELP, Pre
CCA distance between layers, YELP, Dense
CCA distance between layers, YELP, Sparse25
CCA distance between layers, YELP, Sparse70
CCA distance between layers, YELP, Sparse95
MSID distance between layers, YELP, Pre
MSID distance between layers, YELP, Dense
MSID distance between layers, YELP, Sparse25
MSID distance between layers, YELP, Sparse70
MSID distance between layers, YELP, Sparse95
AGW distance between layers, YELP, Pre
AGW distance between layers, YELP, Dense
AGW distance between layers, YELP, Sparse25
AGW distance between layers, YELP, Sparse70
AGW distance between layers, YELP, Sparse95
GW distance between layers, Yelp, Pre
GW distance between layers, Yelp, Dense
GW distance between layers, Yelp, Sparse25
GW distance between layers, Yelp, Sparse70
GW distance between layers, Yelp, Sparse95

(a) Pre-trained (b) Dense (c) 25% Sparse (d) 70% Sparse (e) 95% Sparse

Figure 15: Pairwise (layer) distances on Yelp, across different BERT models. Different Rows: *RSA, RSM, CKA, CCA, MSID, AGW, and the proposed GW distance*, from top to bottom. Different columns: first column is the pre-trained BERT and the rest are fine tuned BERT models with increasing sparsity (dense, 25%, 70% and 95% sparsity). As one can be seen, GW clearly demarcates the (functional) sub-network blocks.

## M GW Distance with Different Random Seeds

Neural networks initialized with different random seeds can converge to distinct representations (Li et al., 2015; Morcos et al., 2018; Kornblith et al., 2019), even when their performance is comparable. To study the impact of initialization seeds on the learned representations, we train the same BERT model on YELP datasets with different seeds, with identical hyperparameters for a total of 27,000 iterations. As shown in Figure 19, while the learned representations vary across seeds, but the general block structures remain consistent when analyzed using GW distances.

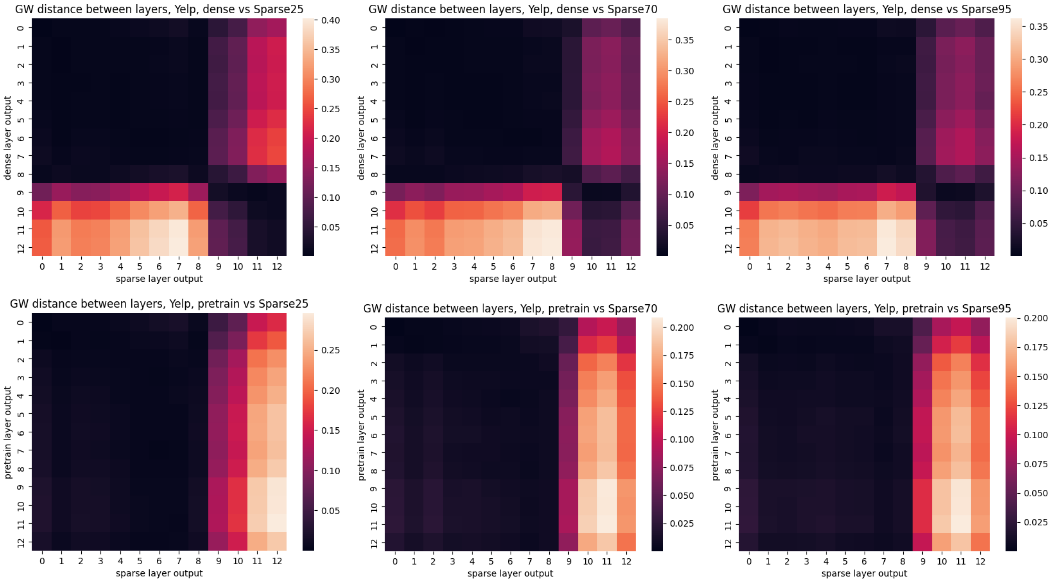

Figure 16: Pairwise distances on YELP dataset, of layers across two different BERT models. *TOP*: Densely fine-tuned BERT model vs fine-tuned BERT models with different sparsity levels. *Bottom*: Pretrained BERT model vs fine-tuned BERT models with different sparsity levels.

## N Computer Vision Application: CIFAR-10 Datasets

In addition to the attention-based architectures, we also test our approach on ResNet9, a popular convolutional neural network architecture(He et al., 2016; Park et al., 2023). We compare a randomly initialized ResNet9 and a trained model on CIFAR 10 image dataset CIFAR-10 (Krizhevsky et al., 2009), achieving 91.63% accuracy on the test data. CIFAR-10 dataset consists of 60000 32x32 color images in 10 image classes, with 6000 images per class. There are 50000 training images and 10000 testing images. The classes are completely mutually exclusive. ResNet is a convolutional neural network with many residual connections. ResNet9 specifically contains 9 convolution layers, each followed by BatchNorm and ReLU activation. The exact details of the ResNet 9 is listed in Table 3.

We show the pairwise distance of all layers in consideration using all methods, that can handle difference dimensions of inputs, in Figure 20. The first column shows results from randomly initialized pre-trained models, and the second columns shows results from the trained ResNet. Pre-trained models generally do not show clear sub-network structures, while the trained models shows differences across layers. RSA, RSM, and CKA show progressive changes over the network layers, which is not too informative. AGW only shows the last a few layers contain significant changes, and MSID distance does not contain clear patterns. In comparison, GW distance shows clear division of 3 or 4 subnetworks.

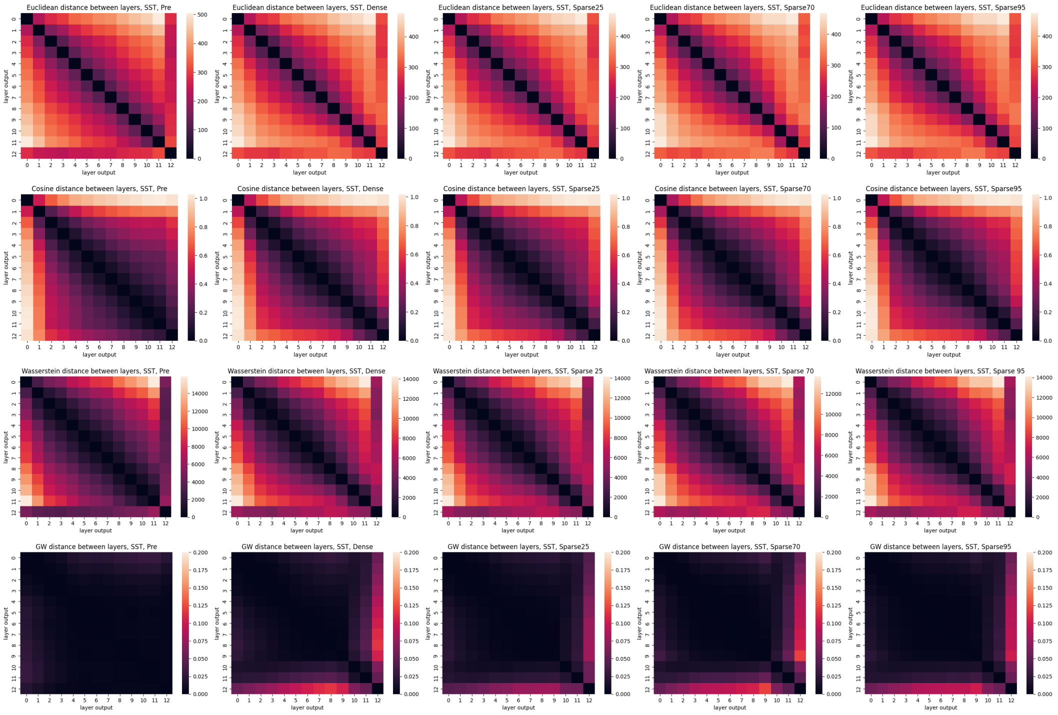

(a) Pretrained (b) Dense (c) 25% Sparse (d) 70% Sparse (e) 95% Sparse

Figure 17: Pairwise distances on SST dataset, across different BERT models. Different Rows: *Euclidean, Cosine, Wasserstein, and the proposed GW distances*, from top to bottom. Different columns: first column is the pre-trained BERT and the rest are fine tuned BERT models with increasing sparsity (dense, 25%, 70% and 95% sparsity).

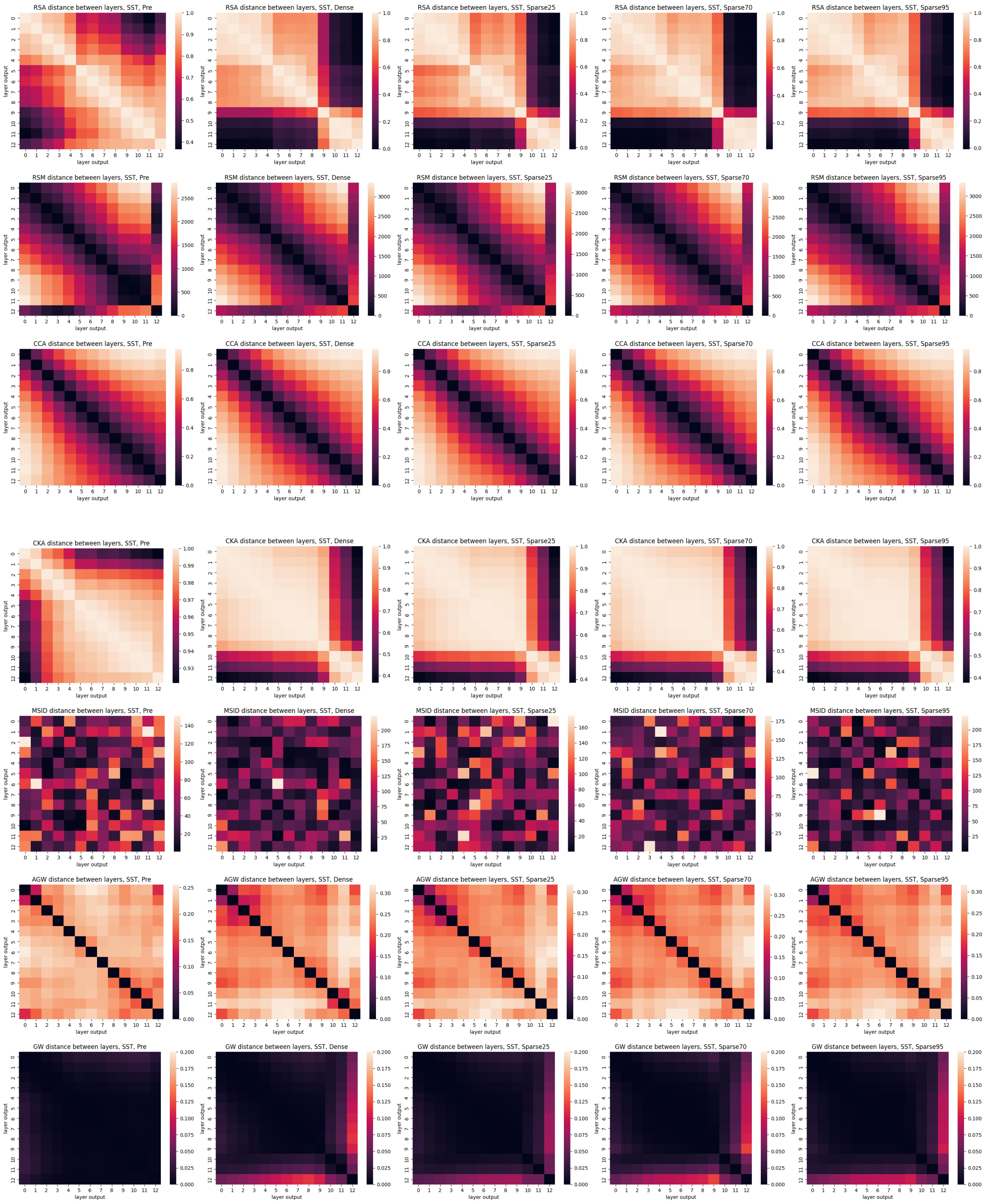

(a) Pretrained (b) Dense (c) 25% Sparse (d) 70% Sparse (e) 95% Sparse

Figure 18: More Pairwise distances on SST dataset, across different BERT models. Different Rows: *RSA, RSM, CCA, CKA, MSID, AGW, and the proposed GW distance*, from top to bottom. Different columns: first column is the pre-trained BERT and the rest are fine tuned BERT models with increasing sparsity (dense, 25%, 70% and 95% sparsity).

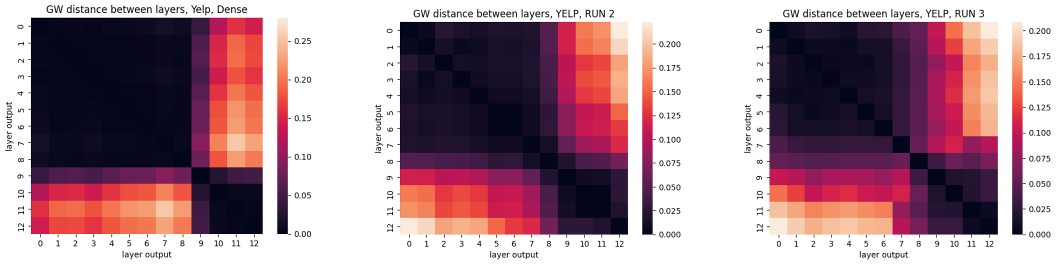

(a) Dense

(b) 25% Sparse

(c) 70% Sparse

Figure 19: Pairwise GW (layer) distances on Yelp, across BERT models trained with 3 different seeds. As one can be seen, the (functional) sub-network blocks stay rather consistent with different seeds even though there is some variations among the models.

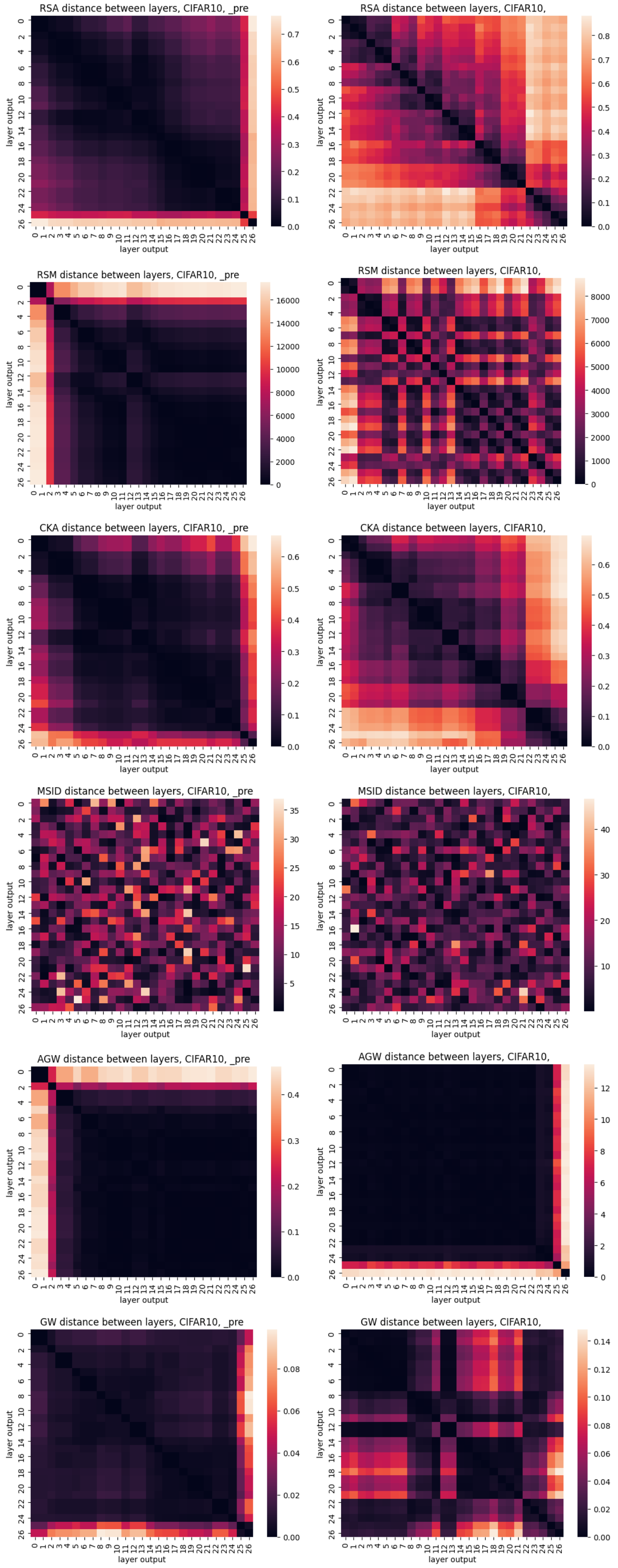

Figure 20: Pairwise (layer) distances on CIFAR-10, across different BERT models. Different Rows: *RSA, RSM, CKA, MSID, AGW, and the proposed GW distance*, from top to bottom. Different columns: first column is the pre-trained ResNet9 and 2nd columns are fine tuned ResNet model.